



MIT Open Access Articles





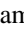
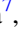







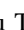

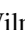
Spectral and Timing Analysis of the Accretion-powered Pulsar 4U 1626–67 Observed with Suzaku and NuSTAR

The MIT Faculty has made this article openly available. **Please share** how this access benefits you. Your story matters.

As Published	10.3847/1538-4357/AB1F87
Publisher	American Astronomical Society
Version	Final published version
Citable link	https://hdl.handle.net/1721.1/132194
Terms of Use	Article is made available in accordance with the publisher's policy and may be subject to US copyright law. Please refer to the publisher's site for terms of use.



Spectral and Timing Analysis of the Accretion-powered Pulsar 4U 1626–67 Observed with *Suzaku* and *NuSTAR*

Wataru B. Iwakiri^{1,13} , Katja Pottschmidt^{2,3} , Sebastian Falkner⁴ , Paul B. Hemphill⁵ , Felix Fürst^{6,14} , Osamu Nishimura⁷ , Fritz-Walter Schwarm⁴ , Michael T. Wolff⁸ , Diana M. Marcu-Cheatham^{2,3} , Deepto Chakrabarty⁵ , John A. Tomsick⁹ , Colleen A. Wilson-Hodge¹⁰ , Matthias Bissinger Kühnel⁴ , Yukikatsu Terada¹¹ , Teruaki Enoto¹² , and Jörn Wilms⁴ 

¹ Department of Physics, Faculty of Science and Engineering, Chuo University, 1-13-27 Kasuga, Bunkyo-ku, Tokyo 112-8551, Japan

² CRESST, Department of Physics, and Center for Space Science and Technology, UMBC, Baltimore, MD 21250, USA

³ NASA Goddard Space Flight Center, Greenbelt, MD 20771, USA

⁴ Dr. Karl-Remeis-Sternwarte and ECAP, Sternwartstr. 7, D-96049 Bamberg, Germany

⁵ MIT Kavli Institute for Astrophysics and Space Research, Massachusetts Institute of Technology, Cambridge, MA 02139, USA

⁶ European Space Astronomy Centre (ESA/ESAC), Science Operations Department, Villanueva de la Cañada (Madrid), Spain

⁷ Department of Electronics and Computer Science, National Institute of Technology (KOSEN), Nagano College, Nagano 381-8550, Japan

⁸ Space Science Division, Naval Research Laboratory, Washington, DC 20375-5352, USA

⁹ Space Sciences Laboratory, University of California, Berkeley, CA 94720, USA

¹⁰ ZP 12 Astrophysics Office, NASA Marshall Space Flight Center, Huntsville, AL 35812, USA

¹¹ Graduate School of Science and Engineering, Saitama University, 255 Shimo-Okubo, Sakura, Saitama 338-8570, Japan

¹² The Hakubi Center for Advanced Research, Kyoto University, Kyoto 606-8302, Japan

Received 2017 November 1; revised 2019 April 29; accepted 2019 May 5; published 2019 June 20

Abstract

We present an analysis of the spectral shape and pulse profile of the accretion-powered pulsar 4U 1626–67 observed with *Suzaku* and *Nuclear Spectroscopic Telescope Array (NuSTAR)* during a spin-up state. The pulsar, which experienced a torque reversal to spin-up in 2008, has a spin period of ~ 7.7 s. Comparing the phase-averaged spectra obtained with *Suzaku* in 2010 and with *NuSTAR* in 2015, we find that the spectral shape changed between the two observations: the 3–10 keV flux increased by $\sim 5\%$, while the 30–60 keV flux decreased significantly by $\sim 35\%$. Phase-averaged and phase-resolved spectral analysis shows that the continuum spectrum observed by *NuSTAR* is well described by an empirical negative and positive power law times exponential continuum with an added broad Gaussian emission component around the spectral peak at ~ 20 keV. Taken together with the observed \dot{P} value obtained from the *Fermi*/gamma-ray burst monitor data, we conclude that the spectral change between the *Suzaku* and *NuSTAR* observations was likely caused by an increase in the accretion rate. We also report the possible detection of asymmetry in the profile of the fundamental cyclotron line. Furthermore, we present a study of the energy-resolved pulse profiles using a new relativistic ray tracing code, where we perform a simultaneous fit to the pulse profiles assuming a two-column geometry with a mixed pencil- and fan-beam emission pattern. The resulting pulse profile decompositions enable us to obtain geometrical parameters of accretion columns (inclination, azimuthal and polar angles) and a fiducial set of beam patterns. This information is important to validate the theoretical predictions from radiation transfer in a strong magnetic field.

Key words: magnetic fields – pulsars: individual (4U 1626–67) – X-rays: binaries

1. Introduction

The magnetic field strengths of neutron stars can be measured directly by observing cyclotron resonance scattering features (CRSFs, or cyclotron lines) in their hard X-ray spectra. Because the parameters of observed CRSFs are determined by the properties of the accreted plasma (e.g., Mészáros 1992; Schönherr et al. 2007; Nishimura 2008; Schwarm et al. 2017a, 2017b), CRSFs in principle provide us with powerful probes of physical processes in strong magnetic fields. This is an active field of research.

The first CRSF was discovered in the X-ray spectrum of Her X-1 by Truemper et al. (1978). To date, CRSFs have been detected from over 20 sources (e.g., Mihara 1995; Caballero & Wilms 2012; Tomsick et al. 2015), with observed magnetic field strengths ranging from 10^{12} to 10^{13} G. The *Nuclear Spectroscopic Telescope Array (NuSTAR)*; Harrison et al. 2013

is an ideal tool to study cyclotron lines, due to its excellent energy resolution and uninterrupted coverage in the energy band relevant for CRSF discoveries (e.g., Fürst et al. 2014; Tendulkar et al. 2014; Bhalerao et al. 2015; Bodaghee et al. 2016; Jaisawal & Naik 2016; Tsygankov et al. 2016). On the other hand, modern theoretical models for cyclotron lines are still not fully in agreement with observations. Theory mostly predicts complex line shapes, with simulated CRSFs showing emission wings and asymmetric profiles. Most observations, however, find CRSFs that are well approximated by smooth, symmetric profiles. For example, Her X-1, one of the brightest CRSF sources on the sky, shows no sign of asymmetry or emission wings in its CRSF profile, as shown by Fürst et al. (2013) using *NuSTAR* and *Suzaku* data. Legitimate cases of asymmetric CRSFs are rare in the observational literature, with the most notable example probably being Cep X-4, which shows extra absorption in its red wing (Fürst et al. 2015). There is also the case of V 0332+53, which may have an asymmetric profile (Pottschmidt et al. 2005), although *NuSTAR* data show that the significance of the asymmetric profile depends on the continuum model (Doroshenko et al. 2017).

¹³ RIKEN MAXI team, 2-1 Hirosawa, Wako, Saitama 351-0198, Japan.

¹⁴ Cahill Center for Astronomy and Astrophysics, California Institute of Technology, Pasadena, CA 91125, USA.

A notable candidate for a complex CRSF profile is 4U 1626–67. This ultracompact X-ray binary (orbital period 42 minutes; see Middleditch et al. 1981; Chakrabarty 1998) hosts a 7.7 s pulsar with a cyclotron line at ~ 37 keV (Orlandini et al. 1998; Coburn et al. 2002; Camero-Arranz et al. 2012; Iwakiri et al. 2012). The pulsar has undergone two torque reversals in recorded history, in 1990 (Chakrabarty et al. 1997) and 2008 (Camero-Arranz et al. 2010), and is currently spinning up. *Suzaku* observations bracketing the torque reversal found no changes in the CRSF parameters, despite a factor of ~ 2.8 increase in X-ray flux and large changes in the soft X-ray spectrum (Camero-Arranz et al. 2012). However, a pulse phase-resolved study of the 2006 *Suzaku* observation (during the spin-down state) by Iwakiri et al. (2012) reported the possible detection of an emission line-like feature at the CRSF energy in the dim phase of the pulse profile. The statistics of the 2010 *Suzaku* observation were too limited to study the CRSF profile in great detail, despite the higher flux.

An analysis of the *NuSTAR* observation of 2015 May by D’Ài et al. (2017, hereafter D17) also showed the CRSF to be asymmetric. D17 models the phase-averaged broadband spectrum obtained by *NuSTAR* and *Swift* with the bulk +thermal comptonization continuum model of Becker & Wolff (2007) and an additional component modeled as disk reflection (Ballantyne et al. 2012) with two CRSFs. The profile of the first 37.95 ± 0.15 keV CRSF is suggested to be complex, and, in contrast to the earlier *Suzaku* analysis (Camero-Arranz et al. 2012; Iwakiri et al. 2012), a second harmonic at 61.0 ± 1.0 keV is claimed.

In this paper we reanalyze the *NuSTAR* and *Suzaku* data from 4U 1626–67 in order to evaluate the significance of the asymmetric line profile of the fundamental CRSF and to perform an analysis of the source behavior using model-independent comparisons of the continuum. In addition, to evaluate the geometry of the accretion column, we perform pulse profile modeling using a new relativistic ray tracing code. Comparing the derived geometrical properties and beam patterns with previous theoretical works, we can achieve an understanding of the physical processes in the strong magnetic field. The *NuSTAR* and *Suzaku* observations and data reductions are introduced in Sections 2.1 and 2.2, respectively. We describe the pulsar’s long-term variability in Section 3.1. In Section 3.2 we model the phase-averaged X-ray spectra using empirical continua and CRSF models. Section 3.3 presents our study of the pulse profile using a new relativistic ray tracing code. Motivated by the pulse profile modeling results, Section 3.4 presents a phase-resolved spectral analysis of the *NuSTAR* spectrum. In Section 4.1 we discuss the implications and origins of the observed spectral and timing changes between the *NuSTAR* and *Suzaku* observations. Section 4.2 investigates the origins of the observed continuum emission. In Section 4.3 we explain the physical interpretation of the pulse profile modeling results, comparing them with previous theoretical results, which take into account the anisotropy of the Thomson scattering cross section in a strongly magnetized plasma. Finally, Section 4.4 presents a comprehensive look at the profile of the fundamental CRSF comparing between observations and between pulse phase intervals.

All spectral analysis in this work was performed with XSPEC, v.12.9.0. Unless stated otherwise, all error bars are at the 90% level for one parameter of interest.

2. Observations and Data Reduction

2.1. NuSTAR Observation of 4U 1626–67

NuSTAR is NASA’s 11th small explorer (SMEX) mission (Harrison et al. 2013). The satellite covers an energy range of 3–79 keV with two CdZnTe detectors, Focal Plane Module A and B (FPMA and FPMB), located at the focal planes of its hard X-ray mirrors. *NuSTAR* observed 4U 1626–67 from 2015 May 4, 12:46 UT, to May 5, 20:27 UT (MJD 57146.5319 to 57147.8521). We reduced the data with version 1.6.0 of the nupipeline software as distributed with HEASOFT 6.19. After standard screening of the data with v20170503 of the *NuSTAR* calibration data, the net exposure time of the observation was 65 ks. A barycentric correction was applied to the arrival time of each event in the FPMA and FPMB with the `barycorr` tool of HEASOFT. We extracted source spectra from FPMA and FPMB using a circle of radius $100''$ centered on the source.

For the timing analysis, the background light curves were extracted from a circular region with a radius of $100''$ at the corner of the *NuSTAR* field of view opposite to the source. For the spectral analysis, we modeled background spectra applying the *NuSTAR* background-fitting and -modeling tool, `nuskybgd` (Wik et al. 2014),¹⁵ using three blank-sky spectra for each telescope extracted from annular regions with radii $300''$ – $400''$, $400''$ – $500''$, and $500''$ – $600''$.

2.2. Suzaku Observation of 4U 1626–67

Suzaku was the fifth Japanese X-ray satellite (Mitsuda et al. 2007). It was equipped with two types of instruments, the X-ray Imaging Spectrometer (XIS; Koyama et al. 2007) and the Hard X-ray Detector (HXD; Takahashi et al. 2007). The XIS was a set of four charge-coupled device cameras at the foci of four X-ray telescopes (Serlemitsos et al. 2007), covering the lower energy band of 0.2–12 keV. XIS 0, XIS 2, and XIS 3 were front-illuminated devices, while XIS 1 was back illuminated. XIS 2 was taken offline after micrometeorite strikes prior to these observations, so we use XIS 0 and XIS 3 (combined: XIS-FI) as well as XIS 1 (XIS-BI) in this analysis. The HXD consisted of PIN silicon diodes (HXD-PIN) and Gd₂SiO₅Ce (GSO) crystal scintillators and covered the 10–600 keV energy band.

The data used here are from the second *Suzaku* observation of 4U 1626–67, which was performed between 2010 September 6, 12:59 UT, and 2010 September 7, 05:42 UT (MJD 55445.5410 to 55446.2375). The first observation of the source had been conducted in 2006 March and was analyzed by Iwakiri et al. (2012). The XIS was operated with the 1/4 window option and standard clocking, which has a time resolution of 2 s. As this is comparable to the 7.7 s pulse period of 4U 1626–67, phase-resolved analysis of the *Suzaku* data is not practical. Therefore, we used the *Suzaku* data for the phase-averaged analysis only. We reprocessed and screened the XIS and HXD data with the standard criteria, using the *Suzaku* reprocessing tool `aepipeline` in the HEASOFT v6.19 package with calibration versions `hxd-20110913`, `xis-20151005`, and `xrt-20110630`. The XIS spectra and light curves were extracted from a circular region with a radius of $4/3$ centered at the source. We accumulated the XIS background spectra from a source-free region. We checked the pile-up

¹⁵ <https://github.com/NuSTAR/nuskybgd>

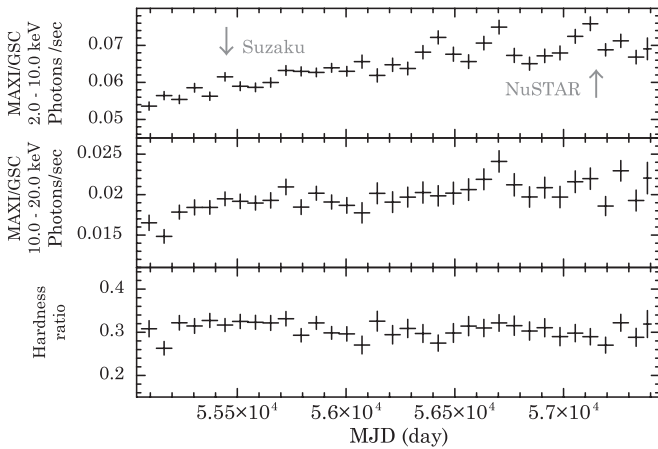


Figure 1. Long-term energy-resolved light curves of 4U 1626–67 obtained with a MAXI/gas slit camera (GSC). Error bars are at the 1σ level. Arrows in the upper panel indicate the dates of the *Suzaku* and *NuSTAR* observations.

effect in the same way as in Yamada et al. (2012) and found that the pile-up fraction was 3% and 1% at 5.7 and 28.7 pixels from the center of the image, respectively. We excluded the regions that show $>1\%$ pile-up fraction so that the pile-up effect is negligible for the subsequent analysis. In this paper, we only used the XIS data down to 3 keV to adjust the energy range of *NuSTAR*.

Because the HXD was not capable of imaging, we applied the simulated non-X-ray background model provided by the *Suzaku* HXD team (Fukazawa et al. 2009) and a cosmic X-ray background, assumed to be the same as the typical model obtained by *HEAO-1* (Boldt 1987). The net exposures were 20.1 ks for the XIS 0, 1, 3 and 18.7 ks for the HXD, respectively. Different screening criteria for South Atlantic Anomaly passages and Earth elevation angles result in different exposures for the XIS and the HXD.

2.3. Long-term Trend of the X-Ray Flux below 20 keV

Figure 1 shows the long-term light curves and hardness ratio of 4U 1626–67 from 2009 October to 2016 January, obtained with MAXI (Matsuoka et al. 2009) on board the *International Space Station* (*ISS*). To avoid any systematic modulation with a period of 70 days caused by the *ISS* orbit, the data are binned to a resolution of 70 days per bin. Over the period considered here, the X-ray fluxes monotonically increased by $\sim 20\%$ in both the 2–10 and 10–20 keV bands, while the hardness ratio remained constant.

3. Analysis and Results

3.1. Timing Analysis

Applying epoch folding (Leahy et al. 1983) to the light curves obtained with the *Suzaku* HXD-PIN and *NuSTAR*, we find the spin period of 4U 1626–67 to be $P_{\text{Suzaku}} = 7.6774(1)$ s and $P_{\text{NuSTAR}} = 7.67295(1)$ s, respectively. These results are consistent with *Fermi*/gamma-ray burst monitor (GBM) results.¹⁶

We estimate the period derivatives, \dot{P} , at the epochs of the *Suzaku* and *NuSTAR* observations by performing a linear fit to the *Fermi*/GBM data for 60 days before and after each observation. The results are $\dot{P}_{\text{Suzaku}} = -2.8 \times 10^{-11} \text{ s s}^{-1}$ and $\dot{P}_{\text{NuSTAR}} = -3.3 \times 10^{-11} \text{ s s}^{-1}$, respectively. Using the conservative

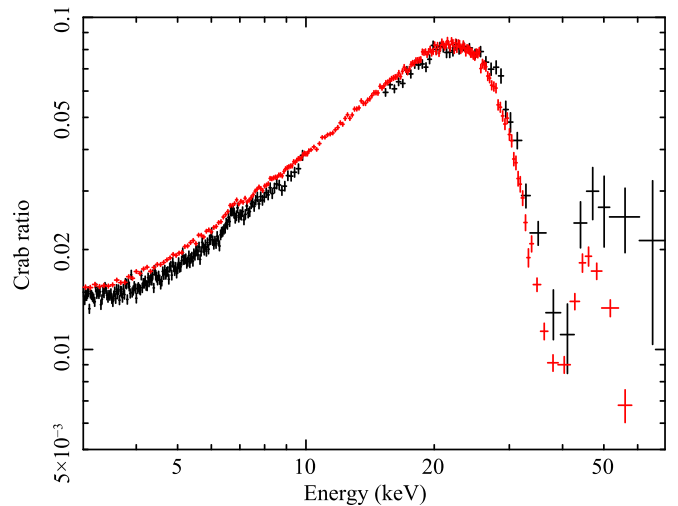


Figure 2. Phase-averaged energy-spectra of 4U 1626–67 divided by the Crab spectrum. Black and red crosses show the data obtained with *Suzaku* (XIS-FI and HXD-PIN) and *NuSTAR* (FPMA), respectively.

approach of Takagi et al. (2016), the uncertainty of these \dot{P} values is $0.2 \times 10^{-11} \text{ s s}^{-1}$. Thus, the period derivative \dot{P} , along with the X-ray flux (Figure 1), increased significantly between the two epochs of the *Suzaku* and *NuSTAR* observations. Accretion torque theory (Ghosh & Lamb 1979) implies that this change in \dot{P} is due to an increase in the accretion rate on the neutron star, consistent with the study of Takagi et al. (2016), who find from observations of 4U 1626–67 spanning 30 yr that the period derivative changes are in good agreement with the prediction by Ghosh & Lamb (1979).

3.2. Phase-averaged Spectral Analysis

3.2.1. Crab Ratio

First, we examine the ratio of the spectra to that of the Crab Nebula and pulsar in order to get a model-independent view of their overall properties. Figure 2 shows the ratio of the phase-averaged spectra obtained by *Suzaku* and *NuSTAR* to that of the Crab, using a canonical model based on the *Suzaku* calibration results¹⁷ as a template for the Crab spectrum. We fixed the cross-normalization factor between XIS 0 and the HXD-PIN to the standard value of 1.16. According to the *NuSTAR* calibration results of Madsen et al. (2017), the cross-normalization factor between the FPMA and *Suzaku*'s instruments are 0.99 ± 0.01 for XIS 0 and 1.13 ± 0.03 for the HXD-PIN, respectively. Comparing with these results, the cross-normalization uncertainty is at the few-percent level.

The CRSF is clearly visible at ~ 40 keV. The ratios in the soft X-rays below 20 keV show that the X-ray flux obtained with *NuSTAR* is brighter than that obtained with *Suzaku*, which is consistent with the long-term X-ray variation observed by MAXI (Figure 1). Above 30 keV, however, the hard X-ray flux decreased in the latter observation. In addition, the spectral peak energy appears to have slightly changed from ~ 22.5 keV in the 2010 *Suzaku* observation to ~ 21.5 keV in the 2015 *NuSTAR* observation. A similar spectral difference is also reported by D17, who compared the long-term *Swift*/Burst Alert Telescope spectrum with the *NuSTAR* data. D17 suggest

¹⁶ <https://gammaray.nsstc.nasa.gov/gbm/science/pulsars.html>

¹⁷ Using the fits for XIS nominal pointings without XIS 2 found in Section 2.2.2 of <http://www.astro.isas.jaxa.jp/suzaku/doc/suzakumemo/suzakumemo-2008-06.pdf>.

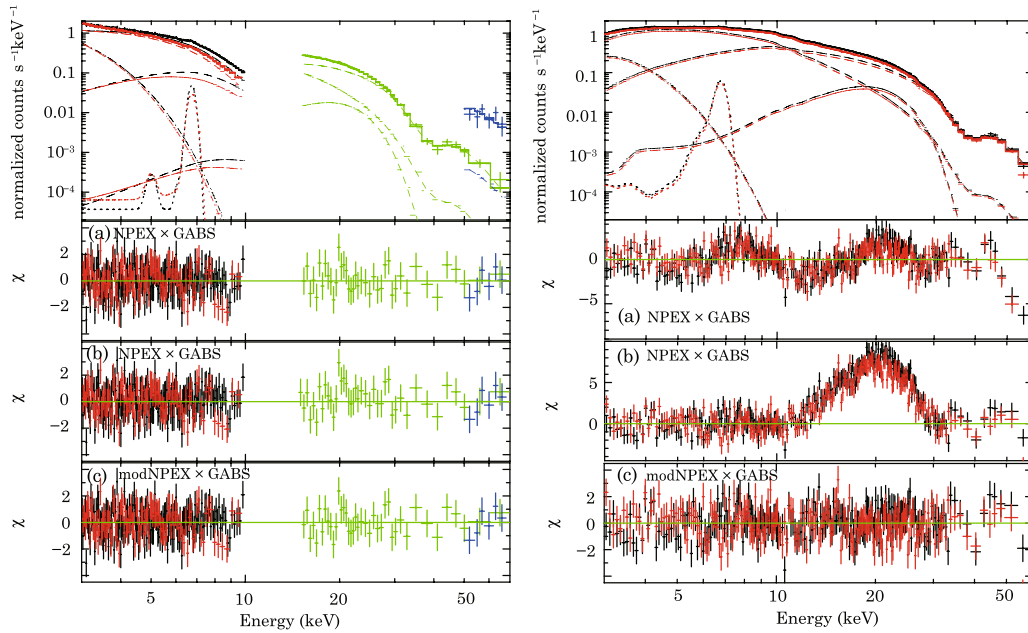


Figure 3. Phase-averaged, background-subtracted spectra of 4U 1626–67 obtained with *Suzaku* (left panel; black, red, green, and blue crosses denote the XIS-FI, XIS-BI, HXD-PIN, and HXD-GSO, respectively) and *NuSTAR* (right panel; black and red crosses indicate the FPMA and FPMB, respectively). The top panel on either side shows the count rate spectra along with the best-fit models: the NPEX with broad Gaussian continuum model (modNPEX, dashed line) with a Gaussian absorption (GABS) model, Fe K α line (dotted line), and an additional blackbody (dashed-dotted line) model (see text and Table 1). The lower three panels show the residuals in units of χ from fitting the data with (a) NPEX with GABS, (b) same model as (a) but the 10–30 keV region was ignored when fitting the model, and (c) modNPEX with GABS.

that the difference is due to a small change of the depth of the fundamental CRSF; however, the model-independent Crab ratios in Figure 2 indicate that changes in the continuum spectral shape should also be considered.

3.2.2. Continuum

Next we modeled the phase-averaged spectra using the negative and positive power law times exponential (NPEX) model (Mihara 1995; Makishima et al. 1999). To model the CRSF, we multiplied the continuum by a Gaussian optical depth absorption model (GABS in XSPEC) $\exp(-S(E))$, where

$$S(E) = \frac{d_a}{\sqrt{2\pi}\sigma_a} e^{-(E-E_a)^2/(2\sigma_a^2)}, \quad (1)$$

and where E_a , σ_a , and d_a are the energy, width, and line depth. We also apply an iron line modeled by an additive Gaussian, and an additional blackbody for the soft excess (Schulz et al. 2001) modeled by a BBODYRAD model, to the *Suzaku* and *NuSTAR* data sets separately. The hydrogen column density is fixed at the total Galactic HI column density ($N_{\text{H}} = 1 \times 10^{21} \text{ cm}^{-2}$).¹⁸

The NPEX model succeeded in reproducing the *Suzaku* data (left of Figure 3(a), with $\chi^2/\text{dof} = 326.08/317$) but failed to reproduce the *NuSTAR* data (right of Figure 3(a), with $\chi^2/\text{dof} = 1005.1/427$). However, we note that it can describe the *NuSTAR* spectrum quite well if the energies around the spectral peak (between 10 and 30 keV) are excluded. Figure 3(b) displays the results of a fit when the 10–30 keV data are ignored. This motivates the construction of a new model, which we term “modNPEX,” consisting of an NPEX

continuum with an additional broad Gaussian emission feature around 20 keV. Similar bumps have been seen in other accretion-powered pulsars (Coburn et al. 2002; Klochkov et al. 2007; Ferrigno et al. 2009; Vasco et al. 2013; Farinelli et al. 2016; Ballhausen et al. 2017). When fitting the *Suzaku* data, the center energy and the width of the Gaussian model were fixed at the best-fit values of the *NuSTAR* data. We found that both data sets are well reproduced by this model (Figure 3(c)). A broad Fe K α emission line is also detected at ~ 6.76 keV with a σ of ~ 150 eV in both the observations. These line centroid energies and widths are consistent with the results in previous papers (Camero-Arranz et al. 2012, *Suzaku* data; D17, *NuSTAR* data). We also tried different phenomenological continuum models, the Fermi–Dirac cutoff model (Tanaka 1986) and a power law modified with a high-energy cut-off (HIGHECUT) model (White et al. 1983; Coburn et al. 2002; Fürst et al. 2013). As a result, we found that the modNPEX is the most successful in providing a good and consistent description of both the phase-averaged and the two phase-resolved spectra (Section 3.4). Therefore, we adopted only the modNPEX as the continuum emission model in this paper.

It should be noted here that D17, using a HIGHECUT model (White et al. 1983; Coburn et al. 2002; Fürst et al. 2013) or bulk+thermal comptonization continuum model (Becker & Wolff 2007), noted absorption-like residuals around ~ 60 keV. They therefore added a second Gaussian absorption model to describe this feature, which they interpret as the harmonic of the CRSF. However, as D17 acknowledge, the centroid energy of the feature deviates significantly from an integer multiple of the fundamental energy, quite a bit more than one expects for a harmonic CRSF (even if relativistic corrections are taken into account, the harmonic should lie at roughly twice the energy of the fundamental; see Pottschmidt et al. 2005). Additionally, the

¹⁸ <https://heasarc.gsfc.nasa.gov/cgi-bin/Tools/w3nh/w3nh.pl>

line parameters are model dependent: D17 find a significantly lower energy of 61 ± 1 keV when using the Becker & Wolff (2007) physical continuum model, compared with their HIGHECUT fits (67 ± 3 keV), while the line depth drops from 50_{-10}^{+17} to 22 ± 5 .

In our analysis of the *NuSTAR* spectra, a second GABS feature is not needed to obtain an acceptable fit. Additionally, even when residuals around 60 keV are present, they are limited to a single bin at the extreme upper end of the useful *NuSTAR* spectrum. Thus, the feature reported by D17 is mainly constrained by the *Swift*-BAT spectrum. We further note that the *Swift*-BAT has a tagged ^{241}Am calibration source on board, which emits 59 keV photons (Gehrels et al. 2004); this contributes to its background and could result in line-like features. Thus, further study of 4U 1626–67 with energy coverage considerably higher than 60 keV is needed to properly study any possible harmonic CRSF.

As the Crab ratios from Section 3.2.1 suggest, our spectral modeling shows a decrease in the pseudo-plasma temperature kT from $7.1_{-0.4}^{+0.6}$ keV to 5.9 ± 0.1 keV, while the CRSF is narrower and shallower in the *NuSTAR* observation compared with *Suzaku*. The unabsorbed X-ray fluxes in the 3.0–10.0, 30.0–60.0, and 3.0–60.0 keV bands derived with the modNPEX model fitting of the *Suzaku* data are $3.21_{-0.12}^{+0.09} \times 10^{-10}$, $1.72_{-0.28}^{+0.31} \times 10^{-10}$, and $1.29_{-0.14}^{+0.14} \times 10^{-9}$ erg cm $^{-2}$ s $^{-1}$, respectively. Assuming a distance of 10 kpc (optical observations constrain its distance to 5–13 kpc; Chakrabarty 1998), these fluxes correspond to an X-ray luminosity of $1.54_{-0.17}^{+0.17} \times 10^{37}$ erg s $^{-1}$ in the 3.0–60.0 keV band. The *NuSTAR* fluxes in the same energy ranges are $3.44_{-0.06}^{+0.04} \times 10^{-10}$, $1.14_{-0.08}^{+0.07} \times 10^{-10}$, and $1.25_{-0.04}^{+0.05} \times 10^{-9}$ erg cm $^{-2}$ s $^{-1}$, corresponding to an X-ray luminosity of $1.50_{-0.05}^{+0.06} \times 10^{37}$ erg s $^{-1}$ in the 3.0–60.0 keV band. Comparing the observed X-ray fluxes by *Suzaku* with the *NuSTAR* results, we found that the 3.0–10.0 keV flux increased by $\sim 5\%$, whereas the 30.0–60.0 keV flux decreased by $\sim 35\%$.

3.2.3. An Asymmetric Cyclotron Line

The residuals of the modNPEX fit to the *NuSTAR* data show a slight systematic structure remaining at around the fundamental CRSF energy (Figure 3(c), right). The presence of a complex line profile for the fundamental CRSF is consistent with D17, despite their different approach to modeling the spectrum. We tried different models to reproduce this feature better and investigate its shape. First, we replaced the GABS model by a pseudo-Lorentzian absorption model (CYAB model, `cyclabs` in XSPEC) and fitted the spectrum using modNPEX as a continuum model. As can be seen in Figure 4 and Table 2, this model did not improve the fit relative to the GABS CRSF model. Next, we added another GABS model, as has been used for V 0332+53 (X 0331+53) (Kreykenbohm et al. 2005; Pottschmidt et al. 2005; Nakajima et al. 2010) and Cep X-4 (Furst et al. 2015). With this model, we successfully eliminated the residuals around the CRSF (Figure 4 and Table 2). These results are largely consistent with D17, although they tie the line energies of the GABS models to having the same values.

However, because the GABS model only produces an absorption feature, we also tried replacing the second GABS component with an additive Gaussian model (i.e., [modNPEX + Gaussian] \times GABS), allowing the Gaussian normalization to be

Table 1
Best-fit Parameters for the Phase-averaged *Suzaku* and *NuSTAR* Spectra of 4U 1626–67 Using the modNPEX Continuum Models with One GABS Component to Describe the Fundamental Cyclotron Line

	modNPEX \times GABS	
	<i>Suzaku</i>	<i>NuSTAR</i>
kT_{BB} (keV)	$0.47_{-0.06}^{+0.06}$	$0.47_{-0.04}^{+0.04}$
A_{BB}^{a}	258_{-104}^{+271}	254_{-85}^{+174}
α	$0.53_{-0.18}^{+0.16}$	$0.47_{-0.10}^{+0.09}$
kT_{NPEX} (keV)	$7.1_{-0.4}^{+0.6}$	$5.9_{-0.1}^{+0.1}$
$A_{\text{n}}(\times 10^{-2})^{\text{b}}$	$2.3_{-0.6}^{+0.7}$	$2.6_{-0.4}^{+0.4}$
$A_{\text{p}}(\times 10^{-5})^{\text{b}}$	$4.0_{-1.8}^{+1.4}$	$7.0_{-1.3}^{+0.9}$
E_{Gaussian} (keV)	19.8(fix)	$19.8_{-0.5}^{+0.4}$
σ_{Gaussian} (keV)	4.8(fix)	$4.8_{-0.5}^{+0.6}$
$A_{\text{Gaussian}}(\times 10^{-3})^{\text{d}}$	$1.8_{-1.7}^{+2.3}$	$3.1_{-0.8}^{+1.2}$
E_{Fe} (keV)	$6.75_{-0.06}^{+0.06}$	$6.76_{-0.05}^{+0.05}$
σ_{Fe} (keV)	$0.13_{-0.08}^{+0.06}$	$0.15_{-0.06}^{+0.06}$
$A_{\text{Fe}}(\times 10^{-4})^{\text{c}}$	$1.3_{-0.4}^{+0.5}$	$1.2_{-0.2}^{+0.3}$
E_{CRSF} (keV)	$38.2_{-0.8}^{+0.9}$	$37.7_{-0.1}^{+0.1}$
σ_{CRSF} (keV)	$5.1_{-0.7}^{+0.7}$	$4.2_{-0.1}^{+0.1}$
d_{CRSF}	$22.9_{-2.6}^{+5.7}$	$14.7_{-0.8}^{+0.8}$
$C_{\text{XISBI}}^{\text{d}}$	$0.941_{-0.007}^{+0.007}$...
$C_{\text{FPMB}}^{\text{e}}$...	$1.002_{-0.002}^{+0.002}$
χ^2/dof	323.48/316	533.08/422
$p_{\text{null}}^{\text{f}}$	3.7×10^{-1}	1.9×10^{-4}

Notes.

^a R_{km}^2/d_{10}^2 , where R_{km} is the radius of the blackbody in kilometers and d_{10} is the distance in units of 10 kpc.

^b Normalization of the power law, defined at 1 keV in units of photons keV $^{-1}$ cm $^{-2}$ s $^{-1}$.

^c Normalization of the Gaussian, defined in units of photons keV $^{-1}$ cm $^{-2}$ s $^{-1}$.

^d A cross-calibration constant for XIS-BI relative to XIS-FI.

^e A cross-calibration constant for FPMB relative to FPMA.

^f Null hypothesis probability.

both positive and negative. The best-fit normalization using the model is negative at the 5σ level, and the energy was consistent with that found using the $2 \times$ GABS CRSF. To evaluate the chance probability of improvement of adding the extra Gaussian component, we simulated 400,000 data sets using `simftest` in XSPEC. The evaluated chance probability was 6.3×10^{-5} . Therefore, we have possibly detected a complex line profile for the fundamental CRSF in the phase-averaged spectrum.

3.3. Pulse Profile Modeling

Because the energy spectrum of 4U 1626–67 is known to depend strongly on pulse phase (Pravdo et al. 1979; Kii et al. 1986; Iwakiri et al. 2012), we present in these next two sections a detailed phase-resolved study. First, to investigate the geometry of the neutron star quantitatively, we performed pulse profile modeling using a new relativistic ray tracing code. Due to the low time resolution of the *Suzaku* data below 10 keV, we concentrate on the *NuSTAR* data. Figure 5 shows the energy-resolved and background-subtracted pulse profiles in 11 different energy bands obtained with *NuSTAR*. The pulse profiles strongly depend on energy, with a double-peaked structure below 10 keV, which becomes single peaked and almost sinusoidal in the higher energy bands. The characteristics of the pulse profiles seen by *NuSTAR* are consistent with the *RXTE* results observed in 2010 (Beri et al. 2014).

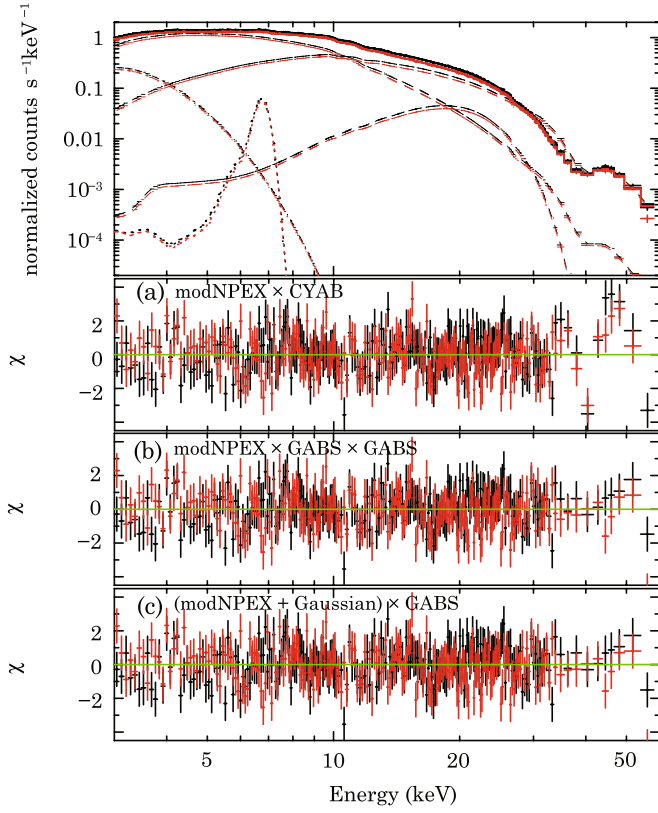


Figure 4. Same *NuSTAR* data as in Figure 3 right panels, but different models are applied. The top panel shows the phase-averaged spectrum with the best-fit model, consisting of a modNPEX continuum with two GABS features, both modeling the fundamental CRSF (see text and Table 2). The lower three panels show the residuals in units of χ from fitting with (a) modNPEX \times CYAB, (b) modNPEX with $2 \times$ GABS, and (c) modNPEX with GABS plus an additional Gaussian.

We use the relativistic light-bending code of Falkner et al. (Falkner et al. 2018a, 2018b, see also Schönherr et al. 2014) to model the energy-resolved pulse profiles of 4U 1626–67 (see Figure 5). This code follows a similar approach to that of Ferrigno et al. (2011) to obtain the observable energy and phase-dependent flux. In contrast to Ferrigno et al. (2011), we are able to apply arbitrary emission patterns to emission regions of any geometrical shape. The code has been used previously by Schönherr et al. (2014) to investigate the energy-dependent phase lags in accreting neutron stars.

In our model for 4U 1626–67 we consider a canonical neutron star of mass $M = 1.4 M_{\odot}$ and radius $R = 10$ km. The observed X-rays are emitted by two cylindrical accretion columns AC1 and AC2 of height $h_{AC1,AC2}$ and radius $r_{AC1,AC2}$. Allowing for an asymmetric magnetic field, the columns are positioned individually at azimuthal angles $\Phi_{AC1,AC2}$ and polar angles $\Theta_{AC1, AC2}$, respectively, in a coordinate system that is measured with respect to the neutron star’s rotational axis. The angle between the line of sight and the neutron star’s angular momentum vector specifies the inclination i of the neutron star. Hence $i = 0^{\circ}$ would correspond to a face-on system.

We make the simplified assumption that the emission pattern of the columns can be described as a mixture of Gaussian-like fan- and pencil-beam emission components in the frame of rest of the neutron star’s surface, e.g., at a given energy the

Table 2
Best-fit Parameters for the Phase-averaged *NuSTAR* Spectra of 4U 1626–67 Using the modNPEX Continuum Models with Different One- and Two-component Models to Describe the Fundamental Cyclotron Line

	modNPEX \times CYAB	modNPEX \times GABS \times GABS	(modNPEX + Gaussian) \times GABS
kT_{BB} (keV)	$0.47^{+0.04}_{-0.04}$	$0.47^{+0.03}_{-0.03}$	$0.47^{+0.03}_{-0.03}$
A_{BB}^a	263^{+167}_{-89}	266^{+154}_{-86}	266^{+155}_{-87}
α	$0.52^{+0.06}_{-0.07}$	$0.48^{+0.05}_{-0.05}$	$0.48^{+0.05}_{-0.05}$
kT_{NPEX} (keV)	$6.3^{+0.1}_{-0.1}$	$5.9^{+0.1}_{-0.1}$	$5.9^{+0.1}_{-0.1}$
$A_n (\times 10^{-2})^b$	$2.6^{+0.3}_{-0.4}$	$2.6^{+0.2}_{-0.2}$	$2.6^{+0.2}_{-0.2}$
$A_p (\times 10^{-5})^b$	$6.1^{+0.7}_{-1.0}$	$7.1^{+0.4}_{-0.4}$	$7.1^{+0.4}_{-0.4}$
$E_{Gaussian}$ (keV)	$20.6^{+0.4}_{-0.6}$	19.8(fix)	19.8(fix)
$\sigma_{Gaussian}$ (keV)	$5.0^{+0.4}_{-0.4}$	4.8(fix)	4.8(fix)
$A_{Gaussian} (\times 10^{-3})^c$	$3.1^{+1.3}_{-0.8}$	$3.1^{+0.3}_{-0.1}$	$3.1^{+0.3}_{-0.1}$
E_{Fe} (keV)	$6.76^{+0.05}_{-0.05}$	$6.76^{+0.05}_{-0.05}$	$6.76^{+0.05}_{-0.05}$
σ_{Fe} (keV)	$0.15^{+0.06}_{-0.06}$	$0.15^{+0.06}_{-0.06}$	$0.15^{+0.06}_{-0.06}$
$A_{Fe} (\times 10^{-4})^c$	$1.2^{+0.3}_{-0.2}$	$1.2^{+0.3}_{-0.2}$	$1.2^{+0.3}_{-0.2}$
E_{CRSF} (keV)	$36.6^{+0.1}_{-0.1}$	$39.9^{+0.6}_{-1.3}$	$39.2^{+0.8}_{-0.7}$
σ_{CRSF} (keV)	$5.3^{+0.3}_{-0.3}$	$2.6^{+0.6}_{-0.8}$	$2.9^{+0.5}_{-0.5}$
τ_{CRSF}	$1.6^{+0.1}_{-0.1}$
d_{CRSF}	...	$5.3^{+5.9}_{-3.8}$	$8.8^{+2.8}_{-3.2}$
E_{abs} (keV)	...	$35.9^{+1.4}_{-2.7}$	$32.8^{+0.9}_{-1.1}$
σ_{abs} (keV)	...	$3.6^{+0.5}_{-0.7}$	$3.4^{+0.5}_{-0.5}$
d_{abs}	...	$8.7^{+4.2}_{-5.6}$...
$A_{abs} (\times 10^{-3})^c$	$-1.2^{+0.4}_{-0.4}$
C_{FPMB}^d	$1.002^{+0.002}_{-0.002}$	$1.002^{+0.002}_{-0.002}$	$1.002^{+0.002}_{-0.002}$
χ^2/dof	596.91/422	508.08/421	507.98/421
p_{null}^e	2.1×10^{-9}	2.3×10^{-3}	2.3×10^{-3}

Notes.

^a R_{km}^2/d_{10}^2 , where R_{km} is the radius of the blackbody in kilometers and d_{10} is the distance in units of 10 kpc.

^b Normalization of the power law, defined at 1 keV in units of photons $\text{keV}^{-1} \text{cm}^{-2} \text{s}^{-1}$.

^c Normalization of the Gaussian, defined in units of photons $\text{keV}^{-1} \text{cm}^{-2} \text{s}^{-1}$.

^d A cross-calibration constant for FPMB relative to FPMA.

^e Null hypothesis probability.

emissivity of one accretion column is given by

$$I_E(\eta) = N_p \exp\left(-\left[\frac{\eta - \bar{\eta}_p}{\sqrt{2}\sigma_p}\right]^2\right) + N_f \exp\left(-\left[\frac{\eta - \bar{\eta}_f}{\sqrt{2}\sigma_f}\right]^2\right), \quad (2)$$

where η is the angle of the emitted photons measured with respect to the magnetic field axis in the frame of rest of the neutron star surface, and where the energy dependent quantities $\bar{\eta}$, σ , and N describe the direction of peak emissivity, the width, and the strength of the pencil-beam (p) and fan-beam (f) components, respectively. For the fan beam we set $\bar{\eta}_f = 90^{\circ}$, i.e., the fan beam is fixed to emit from the sides of the accretion column perpendicular to the B -field. While we impose the same model for the emissivity pattern on both poles, the fluxes of the beams are allowed to vary freely.

We model the energy-dependence of the pulse profile by letting the parameters N , σ , and $\bar{\eta}$ of the emission pattern be energy dependent. For the models described in the following we assume that the emissivity of the accretion column is independent of height and thus constant over the whole

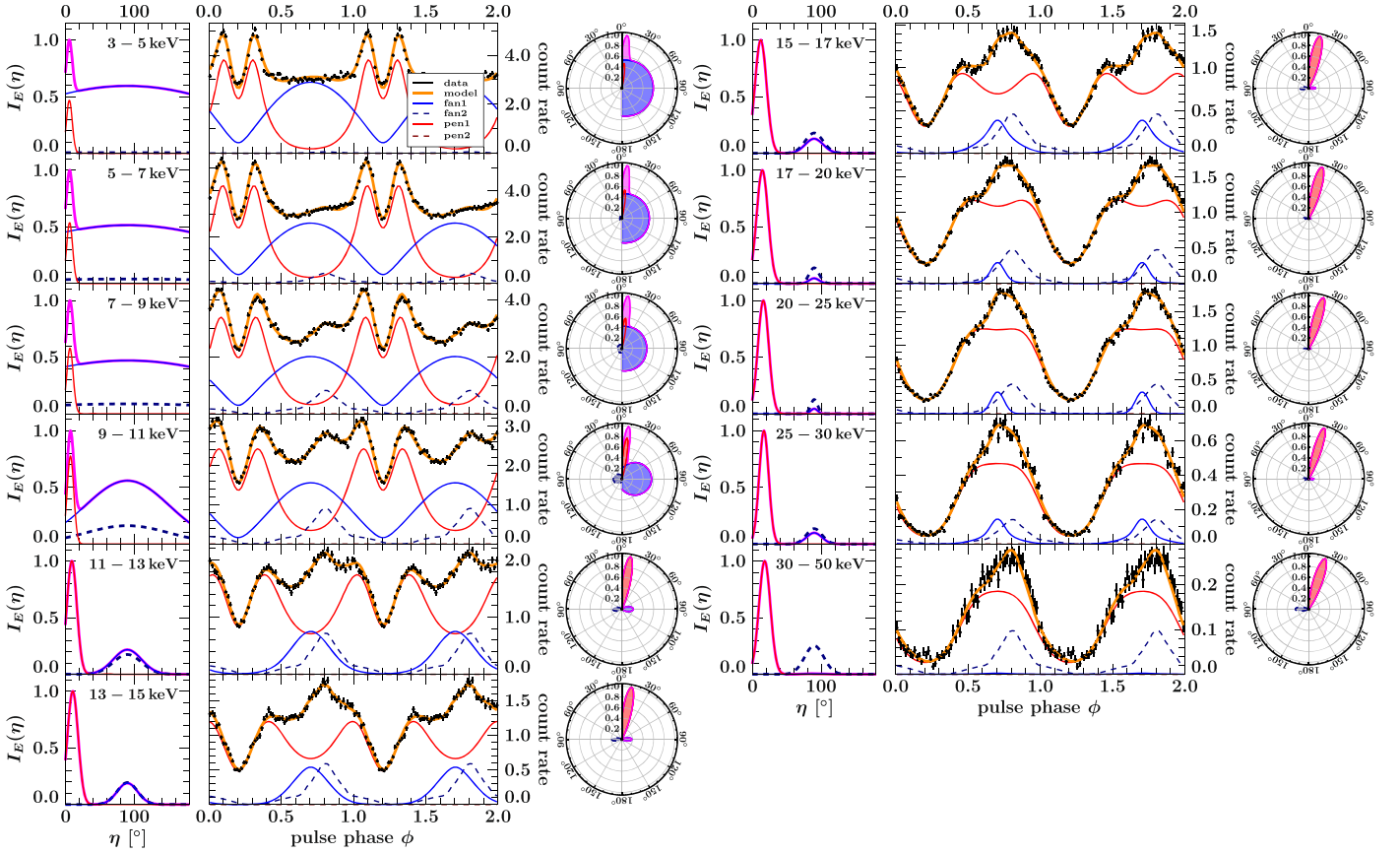


Figure 5. Modeled emission patterns and pulse profiles of 4U 1626–67 in different energy bands. The center panels show the pulse profiles obtained with *NuSTAR* (black points) and the fitted model (orange) with its individual components of the fan (solid blue, dashed navy) and pencil emission (solid red, dashed maroon) of the first and second accretion column, respectively. The left-hand panels show the corresponding normalized emission patterns, $I_E(\eta)$, of the two accretion columns. The solid magenta line corresponds to the combined emission pattern of the fan and pencil beam of the first column. The right-hand panels show the same emission patterns as the polar plot, where the right and left side counting η clockwise and counterclockwise correspond to the first and second accretion column, respectively. The best-fit parameters are shown in Table 3.

column. From Equation (2) we then derive the observed energy- and phase-dependent total flux

$$\mathcal{F}_E(\phi) = F_1(\phi, I_E) + F_2(\phi, I_E), \quad (3)$$

where ϕ is the pulse phase and $F_{1,2}$ is the flux of the individual accretion columns emitting with the given, energy-dependent, emission pattern I_E (Equation (2)). The description of the calculation of $F_{1,2}$, which accounts for all general relativistic effects and is in addition to the parameters here dependent on the neutron star’s inclination, i , is beyond the scope of this paper and is given in Falkner et al. (2018a, 2018b).

Figure 5 includes the best-fit model described above for the energy-resolved and background-subtracted *NuSTAR* pulse profiles in 11 energy bands, which were fitted simultaneously. Lines show the overall model and the individual contributions of the fan and pencil beams from each accretion column. The corresponding parameters are listed in Table 3. The geometrical parameters (i , $\Theta_{AC1,AC2}$, $\Phi_{AC1,AC2}$, $h_{AC1,AC2}$, $r_{AC1,AC2}$) are global, that is, the same for all energies, while the parameters describing the emission profile are determined for each individual energy band. In the best-fit case the size of the second accretion column is tied to the first one, i.e., $r_{AC2} = r_{AC1}$ and $h_{AC2} = h_{AC1}$. Further, the shape of the energy-dependent emission profiles of the two columns are tied together, i.e., $\sigma_{p2} = \sigma_{p1}$, $\bar{\eta}_{p2} = \bar{\eta}_{p1}$ for the pencil-beam component and $\sigma_{f2} = \sigma_{f1}$, $\bar{\eta}_{f2} = \bar{\eta}_{f1} = 90^\circ$ for the fan-beam component. We

found that there are two local minima of the χ^2 landscape of the observer inclination i ; one solution is $i = 9^\circ$, and the other is $i = 27^\circ$. Because the 9° solution shows a simpler pulse profile evolution than the $i = 27^\circ$ solution and because of its consistency with the physical simulation results taking into account the anisotropy of the scattering cross section in a strong magnetic field according to Kii et al. (1986) (see details in Section 4.3), we only show the results from the $i = 9^\circ$ solution in this paper. Table 3 also gives the 90% confidence levels for the parameters. These uncertainties are purely statistical and driven by a complex χ^2 landscape. It is probable that these uncertainties are systematically underestimated. In relation to each other the uncertainties, however, indicate that the radius and height of the column, and for some energies the width of the fan beam, are much less constrained than the other parameters.

The derived best-fit values of $\Theta_{AC1,AC2}$, $\Phi_{AC1,AC2}$ indicate an asymmetric B -field configuration of 4U 1626–67. Such an orientation of a magnetic field axis was also suggested in the previous pulse profile modeling results of Leahy (1991), which show that nine of 20 pulsars require a magnetic field axis offset. The fit shows that the magnetic field of the first column passes through close to the line of sight during each rotation. That is, at pulse phase $\phi = \Phi_{AC1}$, when the first column is in the front, we are looking at the first column from above with an angle to its magnetic field axis of approximately $\Theta_{AC1} - i = 3^\circ$.

Table 3
Fit Parameters of the Accretion Column Model

Global i (deg)	Column ₁				Column ₂		χ^2/dof
	Φ_{AC1} (deg)	Θ_{AC1} (deg)	r_{AC1} (m)	h_{AC1} (m)	Φ_{AC2} (deg)	Θ_{AC2} (deg)	
9.5 ± 0.2	73.6 ± 0.3	$12.50_{-0.11}^{+0.07}$	590 ± 50	252_{-14}^{+12}	290 ± 2	158.1 ± 0.2	1146/631
ΔE (keV)	N_{p1} (cts s ⁻¹)	pencil ₁ σ_{p1} (deg)	$\bar{\eta}_{\text{p1}}$ (deg)	fan ₁ N_{f1} (cts s ⁻¹)	σ_{f1} (deg)	fan ₂ N_{f2} (cts s ⁻¹)	
3–5	$0.95_{-0.02}^{+0.01}$	$4.21_{-0.06}^{+0.07}$	5.73 ± 0.06	$1.21_{-0.02}^{+0.03}$	180_{-16}^{+0}	$0.011_{-0.011}^{+0.013}$	
5–7	1.14 ± 0.02	4.37 ± 0.06	6.12 ± 0.06	$1.09_{-0.02}^{+0.03}$	180_{-26}^{+9}	0.08 ± 0.02	
7–9	$1.03_{-0.02}^{+0.03}$	4.66 ± 0.05	$6.65_{-0.06}^{+0.07}$	$0.84_{-0.04}^{+0.03}$	180_{-67}^{+0}	0.16 ± 0.02	
9–11	$0.83_{-0.03}^{+0.06}$	$4.84_{-0.06}^{+0.05}$	$7.33_{-0.08}^{+0.10}$	$0.60_{-0.06}^{+0.08}$	61_{-10}^{+120}	0.17 ± 0.02	
11–13	$0.77_{-0.09}^{+0.04}$	7.3 ± 0.7	9.4 ± 0.2	$0.17_{-0.04}^{+0.08}$	20_{-6}^{+12}	0.13 ± 0.02	
13–15	$0.56_{-0.03}^{+0.02}$	7.8 ± 0.6	$10.7_{-0.2}^{+0.3}$	$0.11_{-0.02}^{+0.03}$	$14.8_{-0.7}^{+4.0}$	0.11 ± 0.02	
15–17	$0.46_{-0.02}^{+0.03}$	8.4 ± 0.5	12.4 ± 0.4	0.06 ± 0.02	$13.0_{-1.7}^{+0.9}$	0.082 ± 0.009	
17–20	$0.55_{-0.04}^{+0.02}$	8.3 ± 0.3	$14.8_{-0.6}^{+0.3}$	$0.026_{-0.008}^{+0.050}$	7_{-3}^{+6}	0.08 ± 0.01	
20–25	0.53 ± 0.01	7.8 ± 0.2	16.2 ± 0.3	$0.024_{-0.005}^{+0.006}$	$5.0_{-0.3}^{+1.7}$	$0.067_{-0.008}^{+0.007}$	
25–30	$0.18_{-0.03}^{+0.02}$	6.9 ± 0.3	$17.0_{-0.7}^{+0.5}$	$0.02_{-0.01}^{+0.02}$	11_{-5}^{+2}	0.025 ± 0.005	
30–50	$0.070_{-0.008}^{+0.004}$	$8.3_{-0.5}^{+0.6}$	18.1 ± 0.7	≤ 0.007	14_{-8}^{+167}	0.018 ± 0.004	

Note. Parameters not listed here are fixed or tied. In particular we impose $r_{\text{AC1}} = r_{\text{AC2}}$ and $h_{\text{AC1}} = h_{\text{AC2}}$ for the column size, $N_{\text{p2}} = N_{\text{p1}}$, $\sigma_{\text{p2}} = \sigma_{\text{p1}}$, $\bar{\eta}_{\text{p2}} = \bar{\eta}_{\text{p1}}$ for the pencil beam, and $\sigma_{\text{f2}} = \sigma_{\text{f1}}$ and $\bar{\eta}_{\text{f2}} = \bar{\eta}_{\text{f1}} = 90^\circ$ for the fan beam. The given errors correspond to the 90% confidence level.

Furthermore, the displacement of the two accretion columns compared with the symmetric antipodal case is given as

$$\Delta = \pi - \arccos(\mathbf{n}_{\text{AC1}} \circ \mathbf{n}_{\text{AC2}}), \quad (4)$$

which is the angular distance of the two unit vectors, $\mathbf{n}_{\text{AC1,AC2}}$, of the accretion columns positions corresponding to their azimuthal and polar angles. The geometry of our best-fit model yields a displacement of $\Delta = 13.9^\circ$, which represents a moderate asymmetry. In our best-fit model we tie the accretion columns dimensions to prevent parameter degeneracy. Such an asymmetric B -field configuration, however, may suggest columns of different sizes due to possible asymmetric accretion flows, that is, different accretion rates for the two poles (see, e.g., Becker & Wolff 2007; Postnov et al. 2015). Therefore, and due to the fact that we make the very simple assumption of a homogeneously emitting surface, the obtained heights and radii of the columns should not be interpreted as physical quantities.

Despite the simplified assumptions entering the beam pattern, our model describes the observed pulse profiles and their energy evolution remarkably well and with a smooth variation of all relevant parameters of the emission characteristics. The evolution of the pulse profile is characterized by a very wide fan beam, which strongly decreases in width as the energy increases. In contrast, the shape of the pencil-beam component only slightly changes, but the direction of its peak emission changes significantly. This shift explains the widening of the gap between the double peaks in the pulse profile. From 3 to 10 keV the parameters corresponding to the first column change only slightly, but the normalization of the fan beam of the second column increases, explaining the changes seen in the pulse profile at these lower energies. For the geometry in our best-fit model the pencil-beam component of the second accretion column is directed away from the observer over the whole rotational phase and is therefore never

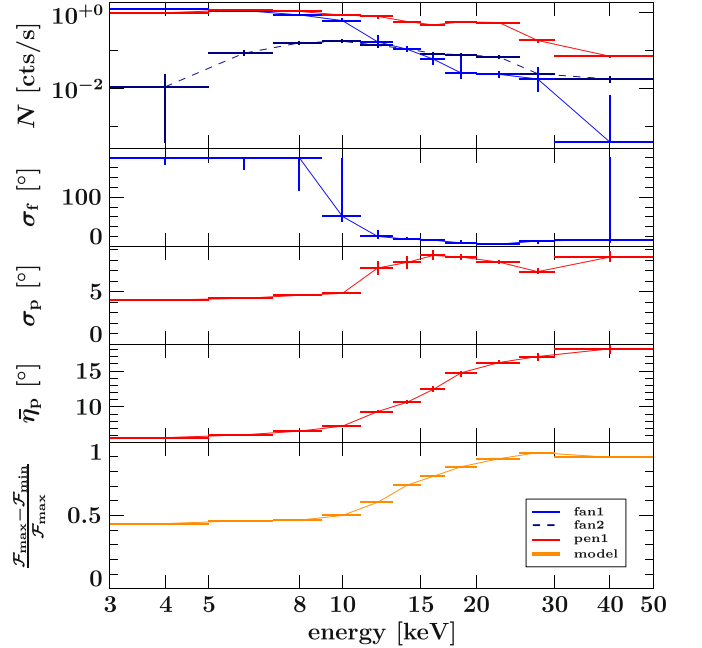


Figure 6. Energy-dependent fit parameters of the accretion column model, with the model's pulsed fraction in the bottom panel. See Table 3 for the best-fit parameters. The panels showing N , σ_f , σ_p , and $\bar{\eta}_p$ include statistical errors (Table 3). Note that the emission angle for the fan beam is fixed at $\bar{\eta}_f = 90^\circ$.

observed. To ensure the correctness¹⁹ of our fit we therefore tie the normalization of the two pencil-beam components, i.e., $N_{\text{p2}} = N_{\text{p1}}$. Figure 6 shows the energy dependency of the parameter values.

The decomposition of the pulse profiles in the middle columns of Figure 5 illustrates how these parameter changes

¹⁹ Otherwise the fit algorithm might be stuck at a $N_{\text{p2}} = 0$ solution, disregarding the second pencil-beam solution also for other tested geometries.

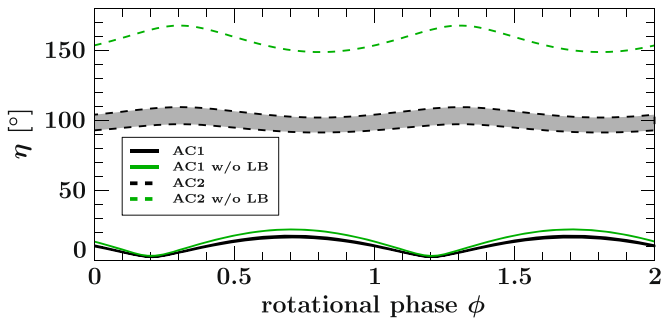


Figure 7. Phase-dependent angle, η , under which the magnetic field is seen at either pole according to the best-fit values in Table 3. Solid and dashed black lines enclose η values corresponding to the first and second accretion column, AC1 and AC2, respectively, accounting for light bending. Green lines show the case of neglecting light bending.

manage to reproduce the pulse profiles so well: the pencil beam is responsible for the distinct and symmetric double peak that characterizes the softer energy bands. The peaks are close together because the pencil beam is directed upward, with only a small offset, $\bar{\eta}_p$, to the magnetic field, which resembles a conical emission pattern. The strong nonpulsed continuum between the two peaks is produced by the broad fan beam, which is shifted by half a phase with respect to the dip between the double peak of the pencil beam. With increasing energy, the double peak decreases in importance and its width broadens while the gap in between increases. This behavior is reflected in the best-fit parameters by showing that the offset angle $\bar{\eta}_p$ and beamwidth σ_p increase with energy (see Figure 6). In addition, the flat plateau at low energies evolves into an asymmetric peak, which is caused by the narrowing of the fan beam. The asymmetry visible in this pulse is caused by the fan beam of the slightly misaligned second accretion column. A consequence of this best-fit geometry is that the pencil beam of the second column is directed away from the observer at all pulse phases, and thus it is not observable. A second consequence is that the evolution of the direction of the peak emissivity of the primary pencil beam, $\bar{\eta}_p$, dominates the evolution of the pulsed fraction, $(\mathcal{F}_{\max} - \mathcal{F}_{\min})/\mathcal{F}_{\max}$, while the width of the fan beam, σ_f , has only a minor influence (Figure 6).

We note that extrapolating the behavior of the pencil and fan beams to even lower energies than considered here predicts an evolution of the pulse profile toward a shape dominated by the single broad hump of the fan beam, consistent with the pulse profiles seen by *XMM-Newton* (Krauss et al. 2007) and *Chandra* (Hemphill et al. 2017).

Modeling the pulse profiles also yields our viewing angle, η , onto the two accretion columns. This parameter is important for the interpretation of the CRSF, the shape of which strongly depends on the angle under which we see the magnetic field (Schwarm et al. 2017a, 2017b). As shown in Figure 7, η is strongly influenced by the effect of light bending, for the first column η varies between 5° and 22° in a small band with mean width $\sim 1^\circ$, whereas for the second column the mean width of the band is $\sim 11^\circ$ between 91° and 110° .

Compared with other models put forward for explaining the energy-dependent change of the pulse profile of 4U 1626–67, our pulse decomposition explains the observed energy-dependent behavior solely by a change in the emission characteristics of the accretion column, without invoking foreground effects, such as the absorption by an accretion stream proposed by Beri et al. (2014). The simpler explanation

is possible by virtue of the low inclination of $i = 9.5^\circ$, where relativistic effects allow a complex interplay between the pencil and fan beam to produce the observed profiles. Although there is some systematic uncertainty in the derived inclination angle due to the complexity of the pulse profile modeling, we note that the inclination is in reasonable agreement with the face-on inclination of $\lesssim 8^\circ$ inferred by studies of the orbit of the system that assume that the donor star is a $0.08 M_\odot$ hydrogen-depleted and partially degenerate star (Levine et al. 1988; Verbunt et al. 1990; Chakrabarty 1998).

The inclination is in moderate disagreement, however, with the $i \lesssim 33^\circ$ estimate for a $0.02 M_\odot$ helium or carbon–oxygen white dwarf donor (Verbunt et al. 1990; Chakrabarty 1998). This higher inclination case is supported by the presence of a complex of broad, double-peaked emission lines around 1 keV (Schulz et al. 2001; Krauss et al. 2007), which are consistent with an inclination in the range of 30° – 40° (Schulz et al. 2013; Hemphill et al. 2017). The low inclination found by our pulse profile modeling can possibly be reconciled with the high inclination implied by the disk lines if the angular momenta of the accretion disk and neutron star are misaligned. This would result in a strong warp in the accretion disk, which could explain the disk flips that have been invoked to explain the torque reversals of 4U 1626–67 (van Kerkwijk et al. 1998; Wijers & Pringle 1999).

3.4. Phase-resolved Spectral Analysis

Due to the strong angular dependency of the cyclotron scattering cross section, we expect that the continuum emission and CRSF profile will depend on our viewing direction (see, e.g., Mészáros 1992). Here we perform a phase-resolved analysis to investigate how the spectral parameters change with phase. Phase-resolved spectroscopy of the *NuSTAR* data was explored in D17, however, their 20 phase bins had poor photon statistics, which precluded a detailed study of the fundamental CRSF. Motivated by our pulse profile modeling results, we instead divide the events into two phase intervals: $\phi = 0.0$ – 0.5 , which is more dominated by soft X-ray flux and contains the double peaks seen at low energies, and 0.5 – 1.0 , where the profile is flat at low energies and more dominated by hard X-ray flux. Based on our pulse profile modeling, the phase 0.0 – 0.5 interval corresponds to viewing angles η of the first accretion column between 5° and 16° , while the 0.5 – 1.0 interval corresponds to angles between 17° and 22° .

3.4.1. Crab Ratio

Similar to our treatment of the phase-averaged data, we first performed a model-independent study of the phase-dependent data using Crab ratios. The normalized phase-resolved spectra by the canonical model of the Crab are shown in Figure 8. It is clear that the continuum emission and CRSF profile both depend strongly on the spin phase, with phases 0.5 – 1.0 being considerably harder spectrally than the 0.0 – 0.5 interval.

3.4.2. Continuum and Cyclotron Line

We model the phase-resolved spectra with the modNPEX continuum models, which are successful in reproducing the phase-averaged spectra (Section 3.2.2). Due to the lower signal-to-noise ratio of the spectra, the iron line energy and width and those of the broad Gaussian component for the

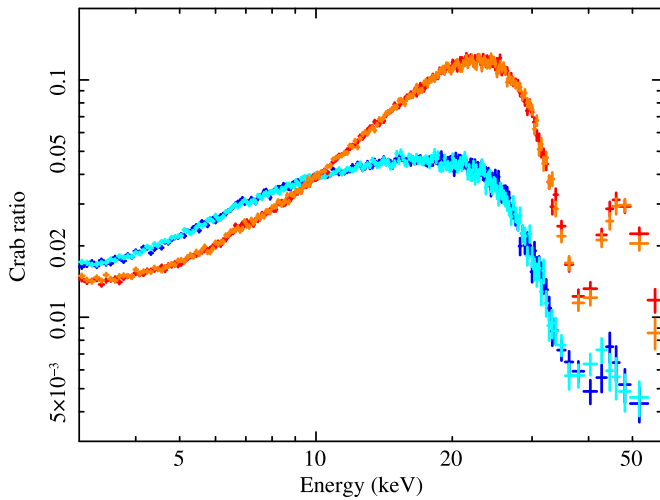


Figure 8. The phase-resolved energy spectra normalized with a canonical model of the Crab (Crab Nebula and pulsar) spectrum. Red and orange crosses show the FPMA and FPMB spectra, respectively, extracted from phase interval $\phi = 0.5\text{--}1.0$ in Figure 5, while blue and cyan crosses show those from phase interval $\phi = 0.0\text{--}0.5$.

modNPEX model were fixed at the values from the phase-averaged spectrum (the *NuSTAR* results in Table 1).

Figure 9 shows the results of the spectral fitting of the spectrum accumulated for phase interval $\phi = 0.0\text{--}0.5$. We do obtain a good fit with the modNPEX continuum and find that a single GABS component (Figure 9) is sufficient to reproduce the CRSF profile.

We then fitted the spectrum from phase interval $\phi = 0.5\text{--}1.0$ with the same model. The results are displayed in Figure 10. With a single GABS component, V-shaped residuals are still visible around the fundamental CRSF (see Figure 10(a)), similar to our results for the phase-averaged *NuSTAR* spectrum in Section 3.2.3. As before, we tried a CYAB model (a pseudo-Lorentzian profile) in place of the GABS component, but this produced worse fits compared with the GABS CRSF, with $\chi^2/\text{dof} = 651.69/427$ (Figure 10(b)). We then tried another GABS component (i.e., modNPEX \times GABS \times GABS) and an additive Gaussian component ((modNPEX + Gaussian) \times GABS). In both cases, the extra residuals around the CRSF were eliminated (Figures 10(c), (d)), and the Gaussian component normalization is negative at the 5σ level. The probability of this feature arising by chance, determined by simulating 400,000 data sets with *simftest* in XSPEC, is 1.8×10^{-5} . The best-fit parameters using the modNPEX model are summarized in Table 4.

Hence, we conclude that we have again tentatively detected the distorted CRSF, which cannot be represented by a simple Gaussian or pseudo-Lorentzian absorption model, similar to the CRSF seen in the phase-averaged *NuSTAR* spectrum.

3.4.3. Dim Phase Spectrum

Iwakiri et al. (2012) reported the possible detection of an emission line-like feature in the dim phase ($\phi = 0.125\text{--}0.250$ in Figure 5) of 4U 1626–67 during the spin-down state. We extracted a spectrum from this phase interval and fitted it with the modNPEX model; the results are displayed in Figure 11(a) and Table 5. The spectrum is well reproduced by only the continuum model—the CRSF feature does not appear in the

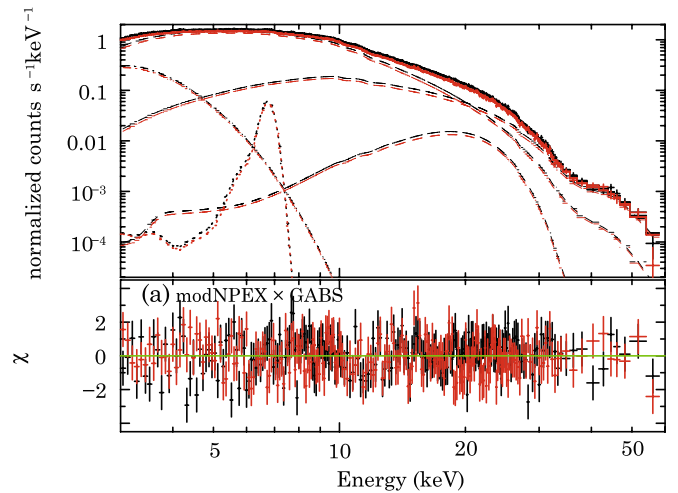


Figure 9. Phase-resolved spectra extracted from the phase interval $\phi = 0.0\text{--}0.5$ as defined in Figure 5 (black and red crosses for FPMA and FPMB, respectively) with the best-fit model consisting of modNPEX with a GABS component. The lower panels show χ residuals of the best-fit results for the models of (a) modNPEX with GABS.

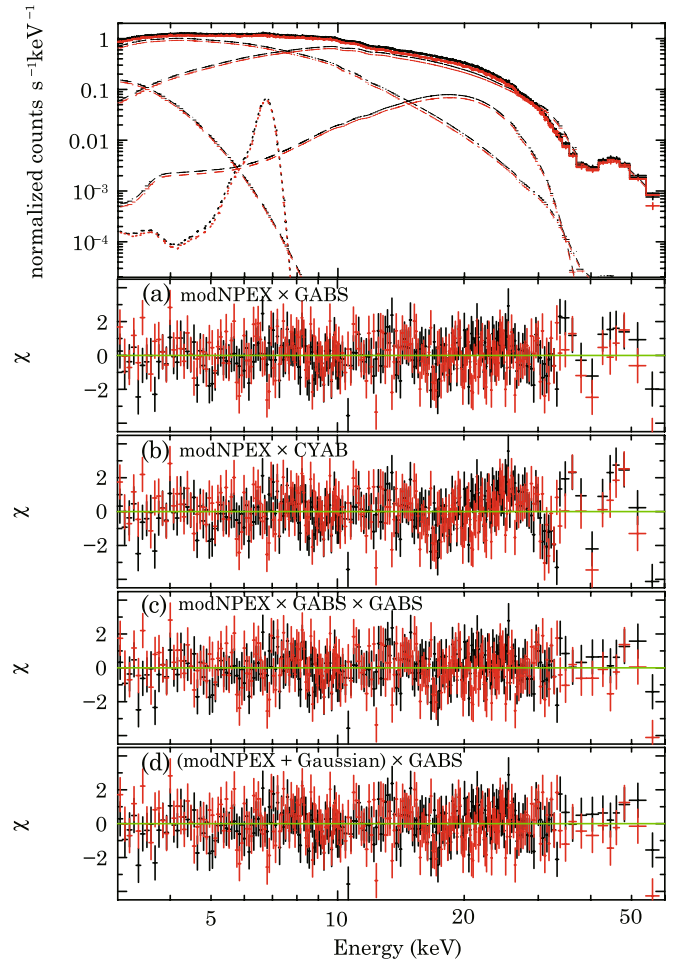


Figure 10. Phase-resolved spectra extracted from the phase interval $\phi = 0.5\text{--}1.0$ as in Figure 5 (black and red crosses for FPMA and FPMB, respectively) with the best-fit model consisting of modNPEX with two GABS components. The lower panels show χ residuals of the best-fit results using (a) modNPEX with GABS, (b) modNPEX with CYAB, (c) modNPEX with two GABS, and (d) modNPEX with GABS plus an additional Gaussian.

Table 4
Best-fit Parameters for the Phase 0.0–0.5 and 0.5–1.0 *NuSTAR* Spectra of 4U 1626–67

Pulse phase ϕ	modNPEX \times GABS	modNPEX \times GABS	modNPEX \times GABS \times GABS	(modNPEX + Gaussian) \times GABS
	0.0–0.5		0.5–1.0	
kT_{BB} (keV)	$0.49^{+0.04}_{-0.04}$	$0.42^{+0.07}_{-0.07}$	$0.42^{+0.07}_{-0.07}$	$0.42^{+0.07}_{-0.07}$
A_{BB}^a	244^{+158}_{-85}	352^{+1165}_{-214}	359^{+1026}_{-210}	367^{+1079}_{-217}
α	$0.47^{+0.01}_{-0.01}$	$1.02^{+0.08}_{-0.09}$	$1.00^{+0.08}_{-0.10}$	$1.02^{+0.08}_{-0.09}$
kT_{NPEX} (keV)	$5.6^{+0.3}_{-0.2}$	$6.0^{+0.1}_{-0.1}$	$6.0^{+0.1}_{-0.1}$	$6.0^{+0.1}_{-0.1}$
$A_n(\times 10^{-2})^b$	$1.9^{+0.2}_{-0.2}$	$4.8^{+0.6}_{-0.7}$	$4.7^{+0.7}_{-0.7}$	$4.9^{+0.7}_{-0.7}$
$A_p(\times 10^{-5})^b$	$3.2^{+1.1}_{-1.2}$	$10.3^{+0.3}_{-0.3}$	$12.6^{+0.3}_{-0.3}$	$10.4^{+0.3}_{-0.3}$
E_{Gaussian} (keV)	19.8(fix)	19.8(fix)	19.8(fix)	19.8(fix)
σ_{Gaussian} (keV)	4.8(fix)	4.8(fix)	4.8(fix)	4.8(fix)
$A_{\text{Gaussian}}(\times 10^{-3})$	$1.1^{+0.3}_{-0.3}$	$5.1^{+0.3}_{-0.3}$	$5.5^{+0.3}_{-0.3}$	$5.4^{+0.3}_{-0.3}$
E_{Fe} (keV)	6.76(fix)	6.76(fix)	6.76(fix)	6.76(fix)
σ_{Fe} (keV)	0.15(fix)	0.15(fix)	0.15(fix)	0.15(fix)
$A_{\text{Fe}}(\times 10^{-4})^c$	$1.2^{+0.3}_{-0.3}$	$1.3^{+0.3}_{-0.3}$	$1.3^{+0.3}_{-0.3}$	$1.3^{+0.3}_{-0.3}$
E_a (keV)	$36.5^{+0.5}_{-0.4}$	$37.9^{+0.1}_{-0.1}$	$39.2^{+1.0}_{-0.7}$	$38.9^{+0.5}_{-0.5}$
σ_{CRSF} (keV)	$4.6^{+0.4}_{-0.4}$	$4.0^{+0.1}_{-0.1}$	$2.8^{+0.5}_{-0.5}$	$3.0^{+0.3}_{-0.3}$
d_{CRSF}	$10.8^{+1.7}_{-1.6}$	$15.9^{+0.7}_{-0.7}$	$10.3^{+2.8}_{-5.5}$	$11.7^{+1.7}_{-2.1}$
E_{abs} (keV)	$34.2^{+2.2}_{-1.5}$	$32.5^{+0.7}_{-0.8}$
σ_{abs} (keV)	$2.9^{+0.8}_{-0.5}$	$2.8^{+0.5}_{-0.5}$
d_{abs}	$4.8^{+5.6}_{-2.6}$...
$\text{Norm}_{\text{abs}} \times 10^{-3}$	$-1.4^{+0.5}_{-0.5}$
χ^2/dof	453.52/427	522.50/427	493.80/424	494.55.47/424
p_{null}^d	1.8×10^{-1}	1.1×10^{-3}	1.1×10^{-2}	1.0×10^{-2}

Notes.

^a R_{km}^2/d_{10}^2 , where R_{km} is the radius of the blackbody in kilometers and d_{10} is the distance in units of 10 kpc.

^b Normalization of negative (n) and positive (p) NPEX components, defined at 1 keV in units of photons $\text{keV}^{-1} \text{cm}^{-2} \text{s}^{-1}$.

^c Normalization of the Gaussian, defined in units of photons $\text{keV}^{-1} \text{cm}^{-2} \text{s}^{-1}$.

^d Null hypothesis probability.

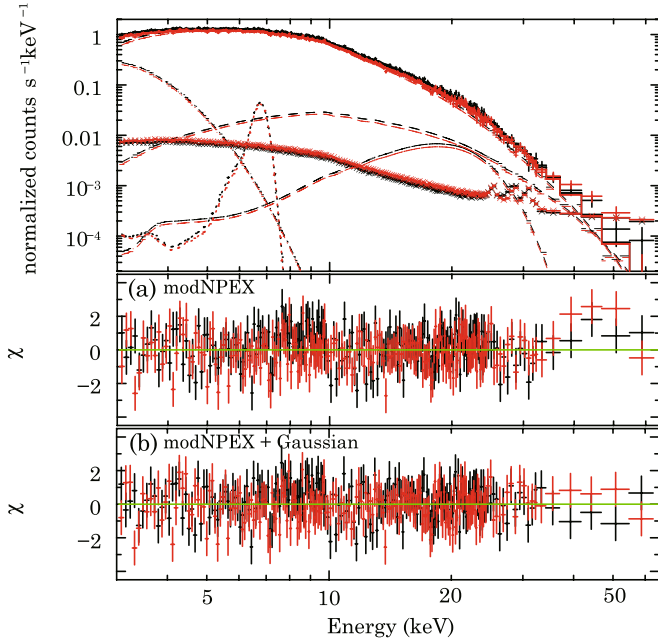


Figure 11. Phase-resolved spectra extracted from the phase interval $\phi = 0.125\text{--}0.250$ defined in Figure 5 (black and red crosses for FPMA and FPMB, respectively) with the best-fit modNPEX model. The background spectra are shown as well (black and red “x” symbols for FPMA and FPMB, respectively). The lower panels show the χ residuals for the best-fit models with (a) a pure modNPEX continuum and (b) modNPEX with an additional Gaussian.

Table 5
Best-fit Parameters for the Phase 0.125–0.250 *NuSTAR* Spectra of 4U 1626–67

	modNPEX	modNPEX + Gaussian emission
kT_{BB} (keV)	$0.41^{+0.05}_{-0.05}$	$0.47^{+0.05}_{-0.05}$
A_{BB}^a	684^{+1250}_{-397}	324^{+424}_{-159}
α	$0.10^{+0.10}_{-0.09}$	$-0.15^{+0.18}_{-0.04}$
kT_{NPEX} (keV)	$5.3^{+0.5}_{-0.5}$	$4.6^{+6.0}_{-0.6}$
$A_n(\times 10^{-2})^b$	$1.6^{+0.2}_{-0.2}$	$1.3^{+0.3}_{-0.2}$
$A_p(\times 10^{-5})^b$	$0.5^{+1.1}_{-0.4}$	< 4.9
E_{Gaussian} (keV)	19.8(fix)	19.8(fix)
σ_{Gaussian} (keV)	4.8(fix)	4.8(fix)
$A_{\text{Gaussian}}(\times 10^{-3})$	$0.5^{+0.2}_{-0.2}$	$1.0^{+0.3}_{-0.3}$
E_{Fe} (keV)	6.76(fix)	6.76(fix)
σ_{Fe} (keV)	0.15(fix)	0.15(fix)
$A_{\text{Fe}}(\times 10^{-4})^c$	$0.8^{+0.5}_{-0.5}$	$0.9^{+0.5}_{-0.5}$
E_a (keV)	...	40.5(fix)
σ (keV)	...	$8.5^{+3.8}_{-2.5}$
Norm ($\times 10^{-4}$)	...	$2.2^{+0.7}_{-0.7}$
χ^2/dof	395.68/384	366.99/382
p_{null}^d	3.3×10^{-1}	7.0×10^{-1}

Notes.

^a R_{km}^2/d_{10}^2 , where R_{km} is the radius of the blackbody in kilometers and d_{10} is the distance in units of 10 kpc.

^b Normalization of negative (n) and positive (p) NPEX components, defined at 1 keV in units of photons $\text{keV}^{-1} \text{cm}^{-2} \text{s}^{-1}$.

^c Normalization of the Gaussian, defined in units of photons $\text{keV}^{-1} \text{cm}^{-2} \text{s}^{-1}$.

^d Null hypothesis probability.

dim phase significantly. However, the residuals around 45 keV do indicate a possible emission line-like feature, although the signal is weak compared with the background level. If we add a Gaussian emission component in the same manner as Iwakiri et al. (2012), with the center energy fixed at their best-fit value $E = 40.5$ keV (Figure 11(b)), the fitted width of $\sigma = 8.5_{-2.5}^{+3.8}$ keV is consistent with the width found in the spin-down state, which showed $\sigma > 4.5$ keV, whereas the normalization of $2.2_{-0.7}^{+0.8} \times 10^{-4}$ photons $\text{cm}^{-2} \text{s}^{-1}$ is lower than the spin-down observation's $8.8_{-2.9}^{+7.2} \times 10^{-4}$ ph $\text{cm}^{-2} \text{s}^{-1}$. The chance probability of improvements of adding this emission feature is 2.0×10^{-2} , determined by simulating 20,000 data sets with `simftest` in XSPEC. Therefore, we concluded that we have only marginally detected the emission line at about the 2σ level. The observed unabsorbed fluxes for the dim phase of the spin-down state and the spin-up state in the 3–60 keV band are $2.2_{-0.2}^{+0.2} \times 10^{-10}$ and $6.0_{-1.0}^{+0.1} \times 10^{-10}$ erg $\text{cm}^{-2} \text{s}^{-1}$, respectively (when we calculate the fluxes, the blackbody parameters are fixed). We note that while D17 claimed the presence of an absorption feature in the dim phase of the pulse, their chosen phase interval is different from ours, corresponding to approximately $\phi = 0.2$ – 0.35 in Figure 5, and thus this discrepancy is not problematic.

4. Discussion

We have presented an analysis of two observations of 4U 1626–67 with *Suzaku* in 2010 September and *NuSTAR* in 2015 May. We have performed broadband spectral analysis, using both phase-averaged and phase-resolved data. In the phase-averaged analysis, we have found a change in the continuum shapes between the observations and confirmed the complex profile of the fundamental CRSF in the *NuSTAR* data suggested by D17. In the phase-resolved analysis using the *NuSTAR* data, we have shown the phase dependence of the continuum and CRSF feature and find further evidence for a distorted CRSF profile during the brighter phase. We have also modeled the energy-resolved pulse profiles using a new relativistic ray tracing code. In this section, we discuss the nature of 4U 1626–67, based on our findings.

4.1. Difference of the Continuum and Pulse Period between the Two Observations

We have found that the continuum emission is different between the 2010 *Suzaku* and 2015 *NuSTAR* observations. Let us consider the implications of this result.

According to Ghosh & Lamb (1979), for accretion via a disk, the rate of change in the pulse period, \dot{P} , is proportional to $\dot{M}^{6/7}$, where \dot{M} is the total mass accretion rate onto the neutron star. Thus, we can estimate the accretion rate onto 4U 1626–67 using \dot{P} from *Fermi*/GBM monitoring. As found in Section 2.3, \dot{P} over the *Suzaku* observation was $-2.8 \times 10^{-11} \text{ s s}^{-1}$, while over the *NuSTAR* observation it was $-3.3 \times 10^{-11} \text{ s s}^{-1}$. The 15% higher \dot{P} during the *NuSTAR* observation would thus imply a 13% higher accretion rate per Ghosh & Lamb (1979).

Based on the Crab ratios of these data sets (Figure 2), as well as our spectral fitting results (Table 1), hard X-ray photons are suppressed in the *NuSTAR* observation relative to the 2010 *Suzaku* spectrum. Because hard X-ray photons are mainly produced by thermal comptonization in the accretion column (Becker & Wolff 2007), we can infer that the electron

temperature of the plasma decreased. However, the photon index α did not change significantly between the observations.

Summarizing our interpretations of our timing and spectral results, the *NuSTAR* observation saw a higher accretion rate and lower temperature in the accretion column compared with the *Suzaku* observation. At least in terms of these results, the spectral variation between the 2010 *Suzaku* and 2015 *NuSTAR* observations indicates that the decrease in the plasma temperature is caused by the increased accretion rate. However, the relation between the accretion rate and the temperature is not simple due to the complex of radiative transfer processes under the strong magnetic field. Future theoretical study is needed to verify our interpretation.

4.2. Origin of the Continuum Emission

The high sensitivity of *NuSTAR* in the hard X-ray band and our analyses of the phase-averaged and phase-resolved spectra lead us to conclude that the most appropriate empirical model for the continuum emission of 4U 1626–67 is the modNPEX model. The results indicate that the extra Gaussian is needed to allow the NPEX model-based fit to provide a good description of the physical continuum. Similar broad Gaussian features have been detected from several other accretion-powered pulsars, e.g., 4U 0115+63, Cen X-3, Her X-1, and A 0535+26 (Suchy et al. 2008; Ferrigno et al. 2009; Vasco et al. 2013; Ballhausen et al. 2017). Because the broad Gaussian feature appears around the spectral peak, it is inferred that the main difference between the simple NPEX continuum model and the observed spectrum is the spectral shape of the quasi-exponential cutoff. The NPEX model approximates the Wien peak-like cutoff, which is expected for a pure thermal comptonization regime, but the shape of the spectral cutoff is mainly determined by the contribution ratio of the bulk and thermal comptonization in their photon propagation process. Moreover, because there are three types of seed photons (bremsstrahlung and cyclotron emission created along the column, blackbody emission from the base of the column), the cutoff shape is also related to the contribution ratio of the seed photons. Therefore, a physical model fitting is important to investigate the origin of the broad Gaussian feature observed from 4U 1626–67. However, this is beyond the scope of the present paper. While D17 did fit 4U 1626–67 with the Becker & Wolff (2007) bulk and thermal comptonization model, their description includes an additional reflection component and the unusual second harmonic absorption feature described earlier. Because of this and because the individual spectral contributions of the different types of comptonized seed photons are not shown, we cannot interpret the 20 keV residual within the D17 picture.

4.3. Origin of the Pulse Profile Evolution

Using our new relativistic ray tracing code, we successfully reproduce the energy-resolved pulse profiles obtained by *NuSTAR* (Section 3.3). We find that the beam pattern is energy dependent. The qualitative explanation for the observed pulse profile evolution is found in the anisotropy of the Thomson scattering cross section in a strongly magnetized plasma. In this case the cross section depends on the photon energy and is different for the ordinary and extraordinary polarization modes. Kii et al. (1986) simulated the 4U 1626–67 pulse profile during spin-up, as obtained by *Tenma* during 1983 May 3–5.

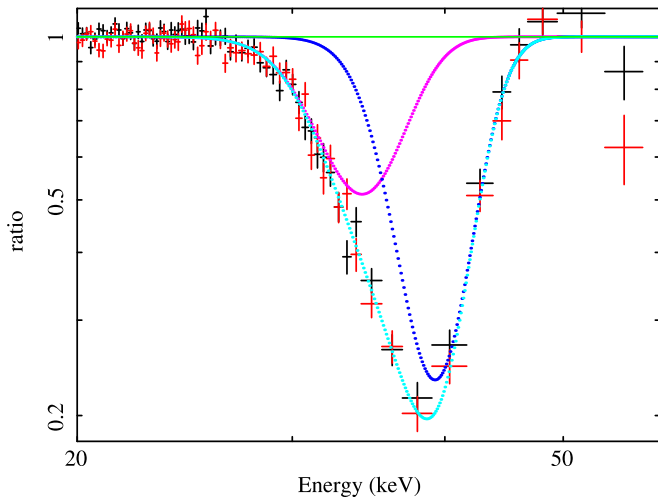


Figure 12. Ratio residuals of the phase $\phi = 0.5\text{--}1.0$ spectra to the continuum component of the best-fit modNPEX model, with the two GABS components excluded (FPMA: black crosses, FPMB: red crosses). Magenta, blue, and cyan dotted lines show the contributions of the primary GABS component, secondary GABS component, and sum of the two GABS models, respectively.

Their simulation is based on anisotropic radiation transfer calculations by Nagel (1981), ignoring vacuum polarization. For a cylindrical geometry with a diameter of the Thomson scattering optical depth $\tau_{\text{Th}} = 80$, Kii et al. (1986) find the following: first, ordinary-mode photons dominate in the lower energy band, whereas extraordinary-mode photons become dominant toward higher energies. Second, the maximum emission angle for extraordinary-mode photons is offset with respect to the magnetic field, and that offset becomes slightly stronger at higher energies. Third, the emission profile with respect to the magnetic field becomes wider at higher energies. Comparing these with our pulse profile modeling results, we can thus draw qualitative connections between our fan-beam evolution and Kii et al.’s (1986) ordinary-mode emission profile and between our pencil-beam evolution and their extraordinary-mode emission profile. Therefore, we suggest that the origin of the observed pulse profile evolution is found in the energy and polarization dependence of the scattering cross section in a strongly magnetized plasma.

X-ray polarimetry will be useful to validate this hypothesis, as ordinary- and extraordinary-mode photons contribute to polarization with opposite signs. Consider, as an example, the future mission *IXPE* (Weisskopf et al. 2016), which will operate in the 2–8 keV band. Under our suggestion that the fan and pencil beams, respectively, correspond to ordinary- and extraordinary-mode photons, Figure 5 predicts that in *IXPE*’s band, the polarization degree will be nearly zero around phase $\phi = 0.45$, where the pencil and fan contributions are comparable, and maximal around phases $\phi = 0.3$ and $\phi = 0.75$, where one beam dominates over the other. Meanwhile, the hard X-ray band covered by, e.g., *X-Calibur* (Beilicke et al. 2014) should find higher overall polarization with a minimum around phase $\phi = 0.7$.

4.4. CRSF Profile

We have found that the observed fundamental CRSF in the phase-averaged and the phase $\phi = 0.5\text{--}1.0$ spectra is better described with a two-Gaussian absorption structure than with a single Gaussian or pseudo-Lorentzian profile (Section 3.4.2).

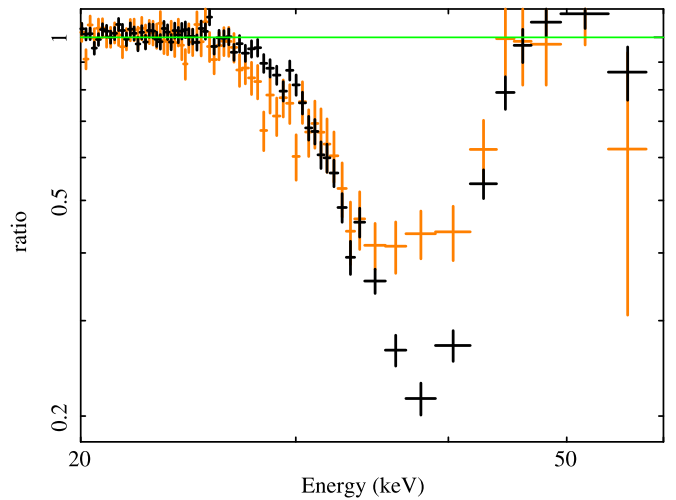


Figure 13. Comparing CRSF shapes between phase $\phi = 0.5\text{--}1.0$ and $\phi = 0.0\text{--}0.5$. These are ratio residuals displayed in the same manner as in Figure 12. Black crosses show the ratio residuals for the phase $\phi = 0.5\text{--}1.0$ FPMA spectrum, while orange crosses show the residuals for phase $\phi = 0.0\text{--}0.5$.

To highlight this asymmetry, we show in Figure 12 the ratio between the data and the continuum component of the best-fit model, where we have excluded the CRSF model. The best-fit two-Gaussian absorption model is overlaid, showing broadening at lower energies. This is similar to what was reported in the *NuSTAR* observation of Cep X-4 (Fürst et al. 2015). Some explanations of this distorted profile have been proposed. For example, Nishimura (2011) proposed that the fundamental line profile becomes asymmetric and shallower toward lower energies due to the superposition of multiple CRSFs produced at different altitudes along the column, assuming some gradient in the density, temperature, and magnetic field. Another interpretation is photon spawning due to inelastic scattering at higher harmonics (Schönherr et al. 2007)—as electrons excited into higher Landau levels cascade down to the ground state, many emitted photons will have similar energy to the fundamental, “filling in” the fundamental line. In addition, our pulse profile modeling suggests that in the phase interval $\phi = 0.5\text{--}1.0$, the second accretion column contributes about 10% of the flux of the first column. Thus, the emission from the second pole may slightly contribute to the CRSF shape. However, a detailed study of the spectra resulting from the mixing of light from the two columns is beyond the scope of this work.

Our phase-resolved spectral analysis also suggests that the CRSF profile depends on the spin phase. We have found that the CRSF in the phase $\phi = 0.0\text{--}0.5$ spectra, which corresponds to the angle $\eta_{\text{AC1}} = 5^\circ\text{--}16^\circ$ (Figure 7), is well reproduced by a simple GABS model. Figure 13 shows a comparison of the CRSF shape between phase $\phi = 0.5\text{--}1.0$ and $\phi = 0.0\text{--}0.5$ in terms of data-to-model ratio (with the absorption components excluded). The depth of the line at $\phi = 0.0\text{--}0.5$ is clearly shallower than at $\phi = 0.5\text{--}1.0$. It is noteworthy that the wings of the two profiles resemble each other, while the core of the $\phi = 0.5\text{--}1.0$ profile appears to be filled in compared with the $\phi = 0.0\text{--}0.5$ profile. To evaluate the width of the CRSF profiles, we calculate the FWHM from these ratios. The results are 12.9 and 11.4 keV, corresponding to $\phi = 0.0\text{--}0.5$ and $\phi = 0.5\text{--}1.0$, respectively. Therefore, the CRSF is wider and shallower between $\eta_{\text{AC1}} = 5^\circ\text{--}16^\circ$ compared with $\eta_{\text{AC1}} = 17^\circ\text{--}21^\circ$ (see Figure 7). The relation between the

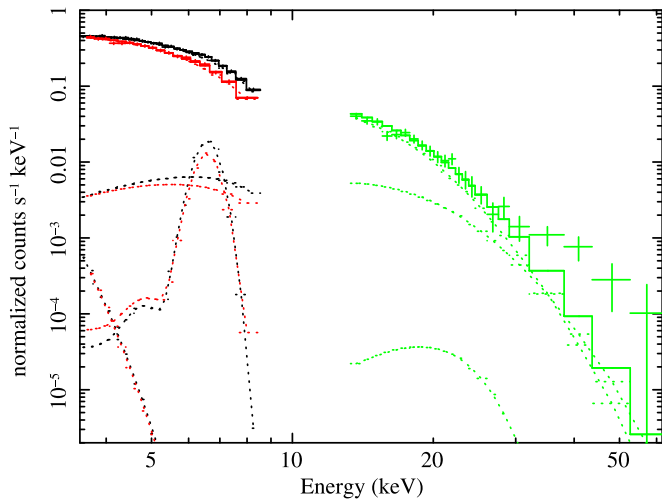


Figure 14. The dim phase spectrum during the spin-down phase of 4U 1626–67 observed by *Suzaku* in 2006 September (Iwakiri et al. 2012) with the modNPEX-based best-fit model. Black, red, and green crosses are the XIS-FI, XIS-BI, and HXD-PIN data, respectively. Histograms show the overall modNPEX-based best-fit model, and dotted lines show individual model components.

CRSF shape and the angle η is qualitatively consistent with theoretical simulations when assuming a slab-type geometry (Isenberg et al. 1998; Schwarm et al. 2017a). The relation is also qualitatively consistent with the theoretical results assuming a cylindrical geometry illuminated by anisotropic injections and magnetic field gradients (Nishimura 2015).

The absorption feature disappears in the dim phase spectrum (phase $\phi = 0.125$ – 0.250). Although an emission line-like feature was detected in the *Suzaku* spectrum observed during the 2006 spin-down state of 4U 1626–67 (Iwakiri et al. 2012), it is only marginally detected in the *NuSTAR* observation (the probability of the feature arising by chance is 2.0×10^{-2}). This fact indicates that the flux of the emission component decreased to the point of nondetectability in the 2015 spin-up state. According to our spectral fits (see Section 3.4.3), the intensity of the emission feature during the *NuSTAR* observation is about four times lower than during the 2006 *Suzaku* observation. On the other hand, the 3–60 keV flux of the *NuSTAR* observation is about three times higher than that of the 2006 *Suzaku* observation. As a consistency check we refitted the 2006 *Suzaku* observation with the same modNPEX model used for the *NuSTAR* observation in Section 3.4.3 (Figure 14). We find consistent results with the emission line-like feature around 40 keV being possibly detected (the probability of this feature arising by chance is 8.0×10^{-4} using 20,000 data sets with *simftest*) and the fitted continuum approximating the exponentially cut-off power law used by Iwakiri et al. (2012) because the contribution of the broad Gaussian and the positive exponential component are comparatively small ($A_{\text{Gaussian}} < 0.4 \times 10^{-3} \text{ keV}^{-1} \text{ cm}^{-2} \text{ s}^{-1}$ and $A_p < 1.5 \times 10^{-5} \text{ keV}^{-1} \text{ cm}^{-2} \text{ s}^{-1}$). According to Section 3.3 the dim phase corresponds to $\eta_{\text{AC1}} \approx 5^\circ$, a viewing angle almost parallel to the magnetic field. Nishimura (2015) specifically addressed 4U 1626–67 and found in simulations that an emission feature could arise at around 50 keV for viewing angles nearly parallel to the magnetic field, which is qualitatively consistent with our observations as well.

5. Summary

We have performed a spectral and timing analysis of the accretion-powered 7.7 s pulsar 4U 1626–67 during its spin-up phase. The results are summarized below:






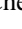







1. The *Fermi*/GBM \dot{P} values during the 2010 *Suzaku* and 2015 *NuSTAR* observations are different, implying a $\sim 15\%$ increase in the spin-up rate.
2. Comparing the phase-averaged 2010 *Suzaku* and 2015 *NuSTAR* spectra we found that in addition to the flux increase below 20 keV, the continua differ significantly from each other above 25 keV, with *NuSTAR* data showing less hard X-ray flux.
3. Based on the changes in flux, \dot{P} , and average spectral shape, we suggest that the accretion rate increased between the *Suzaku* and *NuSTAR* observations, associated with decreasing plasma temperature.
4. Based on the *NuSTAR* data, we confirm earlier results that the pulse profile is strongly energy dependent and changes from being dominated by two narrow peaks in the phase range 0.0–0.5 below 10 keV to being dominated by a single broad peak around pulse phase 0.75 above 20 keV.
5. The CRSF around 37 keV in the phase-averaged and phase 0.5–1.0 *NuSTAR* spectra could not be adequately modeled with a single Gaussian (GABS) or pseudo-Lorentzian (CYAB) optical depth profile. A good description was, however, obtained with two GABS components, leading to an asymmetric profile that is shallower toward lower energies.
6. Possible reasons for an asymmetric CRSF shape are the superposition of line profiles from different locations in the accretion column or the photon spawning effect.
7. We simultaneously modeled the energy-resolved pulse profiles using a new relativistic ray tracing code to evaluate emission patterns. A combination of pencil- and fan-beam emission with a magnetic field nearly aligned with the line of sight reproduces the data well. In this model the narrow double peak in the pulse profile observed below 10 keV in the first half of the pulse profile is caused by a narrow pencil beam with a small offset to the magnetic field, while the flat part of the profile is caused by a fan beam. Toward higher energies the emission geometry of both components evolves (see Figure 5). In particular the offset of the pencil beam regarding the magnetic field enlarges, which causes the double peak to move apart with regard to the phase, increasing its contribution in the second half of the pulse profile.
8. A comparison of our pulse profile modeling with earlier calculations by Kii et al. (1986) shows that the deduced changes in emission pattern may be due to the energy and polarization dependence of the Thomson scattering cross section in a strong magnetic field.
9. The CRSF parameters obtained for the two characteristic pulse phase ranges show that the observed CRSF profile depends significantly on the pulse phase. Moreover, our pulse profile modeling leads us to connect the pulse phase with the angle of the emitted photons measured with respect to the magnetic field axis. Connecting these results, we found that the CRSF width decreases and its

depth increases with increasing emission angle. This relation is expected from theoretical predictions for slab-type geometries (Isenberg et al. 1998; Schwarm et al. 2017a) as well as in asymmetrically illuminated cylindrical-geometry models with a magnetic field gradient (Nishimura 2015).

10. We also checked for the possible presence of a CRSF signature in emission. Such a feature was tentatively reported for the phase 0.125–0.250 (dim phase) spectrum of the 2006 *Suzaku* observation, i.e., the spin-down phase, pre-2008 torque reversal. Such a feature was only marginally detected in the 0.125–0.250 *NuSTAR* spectrum.

The authors appreciate very much the many constructive comments from the anonymous referee. This work is based on data from the *NuSTAR* mission, a project led by the California Institute of Technology, managed by the Jet Propulsion Laboratory, and funded by the National Aeronautics and Space Administration. We thank the *NuSTAR* Operations, Software and Calibration teams for support with the execution and analysis of these observations. This research has made use of the *NuSTAR* Data Analysis Software (NuSTARDAS) jointly developed by the ASI Science Data Center (ASDC, Italy) and the California Institute of Technology (USA). We also thank the *Suzaku*, *Fermi*/GBM and MAXI team members for their dedicated support in satellite operations and calibration. This work has been partially funded by the Deutsche Forschungsgemeinschaft under the DFG grant No. WI 1860/11-1. It uses ISIS functions (ISISscripts) provided by the ECAP/Remeis observatory and MIT (<http://www.sternwarte.uni-erlangen.de/isis/>). The figures in this work have been produced with the S-Lang module `slxfig`. K.P. acknowledges support by NASA's *NuSTAR* Cycle 1 Guest Observer grant No. NNX15AV17G. M.T.W. is supported by the Chief of Naval Research. W.I. is supported by the Special Postdoctoral Researchers Program in RIKEN and JSPS KAKENHI grant No. 16K17717.

ORCID iDs

Wataru B. Iwakiri  <https://orcid.org/0000-0002-0207-9010>
 Katja Pottschmidt  <https://orcid.org/0000-0002-4656-6881>
 Sebastian Falkner  <https://orcid.org/0000-0001-5209-991X>
 Paul B. Hemphill  <https://orcid.org/0000-0002-1676-6954>
 Michael T. Wolff  <https://orcid.org/0000-0002-4013-5650>
 Diana M. Marcu-Cheatham  <https://orcid.org/0000-0001-8061-611X>
 Deepto Chakrabarty  <https://orcid.org/0000-0001-8804-8946>
 John A. Tomsick  <https://orcid.org/0000-0001-5506-9855>
 Colleen A. Wilson-Hodge  <https://orcid.org/0000-0002-8585-0084>
 Matthias Bissinger Kühnel  <https://orcid.org/0000-0002-8709-8236>
 Yukikatsu Terada  <https://orcid.org/0000-0002-2359-1857>
 Teruaki Enoto  <https://orcid.org/0000-0003-1244-3100>
 Jörn Wilms  <https://orcid.org/0000-0003-2065-5410>

References

Ballantyne, D. R., Purvis, J. D., Strausbaugh, R. G., & Hickox, R. C. 2012, *ApJL*, 747, L35
 Ballhausen, R., Pottschmidt, K., Fürst, F., et al. 2017, *A&A*, 608, A105
 Becker, P. A., & Wolff, M. T. 2007, *ApJ*, 654, 435

Beilicke, M., Kislat, F., Zajczyk, A., et al. 2014, *JAI*, 3, 1440008
 Beri, A., Jain, C., Paul, B., & Raichur, H. 2014, *MNRAS*, 439, 1940
 Bhallerao, V., Romano, P., Tomsick, J., et al. 2015, *MNRAS*, 447, 2274
 Bodaghee, A., Tomsick, J. A., Fornasini, F. M., et al. 2016, *ApJ*, 823, 146
 Boldt, E. 1987, in IAU Symp. 124, *Observational Cosmology*, ed. A. Hewitt, G. Burbidge, & L. Z. Fang (Dordrecht: Reidel), 611
 Caballero, I., & Wilms, J. 2012, *MmSAI*, 83, 230
 Camero-Arranz, A., Finger, M. H., Iksanov, N. R., Wilson-Hodge, C. A., & Bekken, E. 2010, *ApJ*, 708, 1500
 Camero-Arranz, A., Pottschmidt, K., Finger, M. H., et al. 2012, *A&A*, 546, A40
 Chakrabarty, D. 1998, *ApJ*, 492, 342
 Chakrabarty, D., Bildsten, L., Grunsfeld, J. M., et al. 1997, *ApJ*, 474, 414
 Coburn, W., Heindl, W. A., Rothschild, R. E., et al. 2002, *ApJ*, 580, 394
 D'Ài, A., Cusumano, G., Del Santo, M., La Parola, V., & Segreto, A. 2017, *MNRAS*, 470, 2457
 Doroshenko, V., Tsygankov, S. S., Mushtukov, A. A., et al. 2017, *MNRAS*, 466, 2143
 Falkner, S., Schwarm, F.-W., Dauser, T., et al. 2018a, *A&A*, submitted
 Falkner, S., Schwarm, F.-W., Kühnel, M., et al. 2018b, *A&A*, submitted
 Farinelli, R., Ferrigno, C., Bozzo, E., & Becker, P. A. 2016, *A&A*, 591, A29
 Ferrigno, C., Becker, P. A., Segreto, A., Mineo, T., & Santangelo, A. 2009, *A&A*, 498, 825
 Ferrigno, C., Falanga, M., Bozzo, E., et al. 2011, *A&A*, 532, A76
 Fukazawa, Y., Mizuno, T., Watanabe, S., et al. 2009, *PASJ*, 61, 17
 Fürst, F., Grefenstette, B. W., Staubert, R., et al. 2013, *ApJ*, 779, 69
 Fürst, F., Pottschmidt, K., Miyasaka, H., et al. 2015, *ApJL*, 806, L24
 Fürst, F., Pottschmidt, K., Wilms, J., et al. 2014, *ApJL*, 784, L40
 Gehrels, N., Chincarini, G., Giommi, P., et al. 2004, *ApJ*, 611, 1005
 Ghosh, P., & Lamb, F. K. 1979, *ApJ*, 234, 296
 Harrison, F. A., Craig, W. W., Christensen, F. E., et al. 2013, *ApJ*, 770, 103
 Hemphill, P. B., Schulz, N. S., Marshall, H. L., & Chakrabarty, D. 2017, From Chandra to Lynx: Taking the Sharpest X-ray Vision Fainter and Farther, Zenodo, doi:10.5281/zenodo.3238548
 Isenberg, M., Lamb, D. Q., & Wang, J. C. L. 1998, *ApJ*, 505, 688
 Iwakiri, W. B., Terada, Y., Mihara, T., et al. 2012, *ApJ*, 751, 35
 Jaisawal, G. K., & Naik, S. 2016, *MNRAS*, 461, L97
 Kii, T., Hayakawa, S., Nagase, F., Ikegami, T., & Kawai, N. 1986, *PASJ*, 38, 751
 Klochkov, D., Horns, D., Santangelo, A., et al. 2007, *A&A*, 464, L45
 Koyama, K., Tsunemi, H., Dotani, T., et al. 2007, *PASJ*, 59, 23
 Krauss, M. I., Schulz, N. S., Chakrabarty, D., Juett, A. M., & Cottam, J. 2007, *ApJ*, 660, 605
 Kreykenbohm, I., Mowlavi, N., Produit, N., et al. 2005, *A&A*, 433, L45
 Leahy, D. A. 1991, *MNRAS*, 251, 203
 Leahy, D. A., Darbro, W., Elsner, R. F., et al. 1983, *ApJ*, 266, 160
 Levine, A., Ma, C. P., McClintock, J., et al. 1988, *ApJ*, 327, 732
 Madsen, K. K., Beardmore, A. P., Forster, K., et al. 2017, *AJ*, 153, 2
 Makishima, K., Mihara, T., Nagase, F., & Tanaka, Y. 1999, *ApJ*, 525, 978
 Matsuoka, M., Kawasaki, K., Ueno, S., et al. 2009, *PASJ*, 61, 999
 Mészáros, P. 1992, *High-energy Radiation from Magnetized Neutron Stars* (Chicago, IL: Univ. Chicago Press)
 Middleditch, J., Mason, K. O., Nelson, J. E., & White, N. E. 1981, *ApJ*, 244, 1001
 Mihara, T. 1995, PhD thesis, Univ. Tokyo (M95)
 Mitsuda, K., Bautz, M., Inoue, H., et al. 2007, *PASJ*, 59, 1
 Nagel, W. 1981, *ApJ*, 251, 288
 Nakajima, M., Mihara, T., & Makishima, K. 2010, *ApJ*, 710, 1755
 Nishimura, O. 2008, *ApJ*, 672, 1127
 Nishimura, O. 2011, *ApJ*, 730, 106
 Nishimura, O. 2015, *ApJ*, 807, 164
 Orlandini, M., Fiume, D. D., Frontera, F., et al. 1998, *ApJL*, 500, L163
 Postnov, K. A., Gornostaev, M. I., Klochkov, D., et al. 2015, *MNRAS*, 452, 1601
 Pottschmidt, K., Kreykenbohm, I., Wilms, J., et al. 2005, *ApJL*, 634, L97
 Pravdo, S. H., White, N. E., Boldt, E. A., et al. 1979, *ApJ*, 231, 912
 Schönherr, G., Schwarm, F.-W., Falkner, S., et al. 2014, *A&A*, 564, L8
 Schönherr, G., Wilms, J., Kretschmar, P., et al. 2007, *A&A*, 472, 353
 Schulz, N. S., Chakrabarty, D., Marshall, H. L., et al. 2001, *ApJ*, 563, 941
 Schulz, N. S., Marshall, H. L., & Chakrabarty, D. 2013, *AAS/High Energy Astrophysics Division*, 13, 126.46
 Schwarm, F.-W., Ballhausen, R., Falkner, S., et al. 2017a, *A&A*, 601, A99
 Schwarm, F.-W., Schönherr, G., Falkner, S., et al. 2017b, *A&A*, 597, A3
 Serlemitsos, P. J., Soong, Y., Chan, K.-W., et al. 2007, *PASJ*, 59, 9
 Suchy, S., Pottschmidt, K., Wilms, J., et al. 2008, *ApJ*, 675, 1487
 Takagi, T., Mihara, T., Sugizaki, M., Makishima, K., & Morii, M. 2016, *PASJ*, 68, S13

- Takahashi, T., Abe, K., Endo, M., et al. 2007, *PASJ*, 59, 35
- Tanaka, Y. 1986, in IAU Coll. 89, Radiation Hydrodynamics in Stars and Compact Objects, Lecture Notes in Physics, ed. D. Mihalas & K.-H. A. Winkler (Berlin: Springer), 198
- Tendulkar, S. P., Fürst, F., Pottschmidt, K., et al. 2014, *ApJ*, 795, 154
- Tomsick, J. A., Bellm, E., Fuerst, F., et al. 2015, arXiv:1501.03534
- Truemper, J., Pietsch, W., Reppin, C., et al. 1978, *ApJL*, 219, L105
- Tsygankov, S. S., Lutovinov, A. A., Krivonos, R. A., et al. 2016, *MNRAS*, 457, 258
- van Kerkwijk, M. H., Chakrabarty, D., Pringle, J. E., & Wijers, R. A. M. J. 1998, *ApJL*, 499, L27
- Vasco, D., Staubert, R., Klochkov, D., et al. 2013, *A&A*, 550, A111
- Verbunt, F., Wijers, R. A. M. J., & Burm, H. M. G. 1990, *A&A*, 234, 195
- Weisskopf, M. C., Ramsey, B., O'Dell, S., et al. 2016, *Proc. SPIE*, 9905, 990517
- White, N. E., Swank, J. H., & Holt, S. S. 1983, *ApJ*, 270, 711
- Wijers, R. A. M. J., & Pringle, J. E. 1999, *MNRAS*, 308, 207
- Wik, D. R., Hornstrup, A., Molendi, S., et al. 2014, *ApJ*, 792, 48
- Yamada, S., Uchiyama, H., Dotani, T., et al. 2012, *PASJ*, 64, 53